ADVANCED MATERIALS INTERFACES
Open Access
www.advmatinterfaces.de

Check for updates

Bioactive Coatings on 3D Printed Polycaprolactone Scaffolds for Bone Regeneration: A Novel Murine Femur Defect Model for Examination of the Biomaterial Capacity for Repair

Karen M. Marshall, Jonathan P. Wojciechowski, Vineetha Jayawarna, Abshar Hasan, Cécile Echalier, Sebastien J. P. Callens, Tao Yang, Janos M. Kanczler, Jonathan I. Dawson, Alvaro Mata, Manuel Salmeron-Sanchez, Molly M. Stevens, and Richard O. C. Oreffo**

Bone tissue engineering seeks to develop treatment approaches for nonhealing and large bone defects. An ideal biodegradable scaffold will induce and support bone formation. The current study examines bone augmentation in critical-sized bone defects, using functionalized scaffolds, with the hypothesized potential to induce skeletal cell differentiation. 3D printed, porous poly(caprolactone) trimethacrylate (PCL-TMA900) scaffolds are applied within a murine femur defect, stabilized by a polyimide intramedullary (IM) pin. The PCL-TMA900 scaffolds are coated with i) elastin-like polypeptide (ELP), ii) poly(ethyl acrylate) (PEA)/fibronectin (FN)/bone morphogenetic protein-2 (PEA/FN/BMP-2), iii) both ELP and PEA/FN/BMP-2, or iv) Laponite nanoclay binding BMP-2. Sequential microcomputed tomography (μCT) and histological analysis are performed. PCL-TMA900 is robust and biocompatible and when coated with the nanoclay material Laponite and BMP-2 induce consistent, significant bone formation compared to the uncoated PCL-TMA900 scaffold. Critically, the BMP-2 is retained, due to the Laponite, producing bone around the scaffold in the desired shape and volume, compared to bone formation observed with the positive control (collagen sponge/BMP-2). The ELP and/or PEA/FN/BMP-2 scaffolds do not demonstrate significant or consistent bone formation. In summary, Laponite/BMP-2 coated PCL-TMA900 scaffolds offer a biodegradable, osteogenic construct for bone augmentation with potential for development into a large scale polymer scaffold for clinical translation.

1. Introduction

Bone tissue engineering has evolved due to the critical need for innovative constructs to replace grafted bone or suboptimal materials currently applied in clinical practice. Defects arising in bone may occur due to trauma, fracture nonunion, infection, resection in oncology cases or congenital conditions.[1] In certain clinical cases, amputation is required as the limb is unsalvageable due to significant soft tissue, vascular, and/or nerve damage.[2] Bone is the second most grafted tissue after blood, frequently using the patient's own bone (autograft) from the iliac crest of the pelvis.[3,4] From a clinical perspective, autograft is the optimal material given it is nonimmunogenic, facilitates osteoinduction due to the presence of growth factors, osteoconduction as bone is a 3D scaffold, and osteogenesis due to the cellular component within.[5] However, there are a number of significant limitations including donor site complications such

K. M. Marshall, J. M. Kanczler, J. I. Dawson, R. O. C. Oreffo
Bone and Joint Research Group
Centre for Human Development
Stem Cells and Regeneration
Institute of Developmental Sciences
University of Southampton
Southampton SO16 6YD, UK
E-mail: k.m.marshall@soton.ac.uk; richard.oreffo@soton.ac.uk

The ORCID identification number(s) for the author(s) of this article can be found under https://doi.org/10.1002/admi.202400389

© 2024 The Author(s). Advanced Materials Interfaces published by Wiley-VCH GmbH. This is an open access article under the terms of the Creative Commons Attribution License, which permits use, distribution and reproduction in any medium, provided the original work is properly cited.

DOI: 10.1002/admi.202400389

J. P. Wojciechowski, C. Echalier, S. J. P. Callens, T. Yang, M. M. Stevens
Department of Materials
Department of Bioengineering
Institute for Biomedical Engineering
Imperial College London
London SW7 2AZ, UK

J. P. Wojciechowski, S. J. P. Callens, T. Yang, M. M. Stevens
Kavli Institute for Nanoscience Discovery
Department of Physiology, Anatomy and Genetics
Department of Engineering Science
University of Oxford
Oxford OX1 3QU, UK

V. Jayawarna, M. Salmeron-Sanchez
School of Engineering, Centre for the Cellular Microenvironment,
Advanced Research Centre
University of Glasgow
Glasgow G11 6EW, UK

as infection, pain and, naturally, limited autograft volume.[6] Thus, the ideal bone substitute material is biocompatible, bioresorbable, osteoconductive, osteoinductive, porous with a comparable structure and strength to bone, easy to use and cost effective.[1] Critically, the material must be able to withstand the complex load and mechanical forces applied, such as weight bearing or mastication.[7]

We have previously assessed the biocompatibility of a poly(caprolactone) trimethacrylate (PCL-TMA900) scaffold material functionalized with a variety of scaffold coatings including elastin-like polypeptides (ELPs), poly(ethyl acrylate) (PEA)/fibronectin (FN)/bone morphogenetic protein-2 (PEA/FN/BMP-2), and the nanoclay Laponite, in vitro, using the chorioallantoic membrane (CAM) assay and in a murine subcutaneous implantation model.[8,9] PCL is a popular polymer due to the biocompatibility and biodegradability. PCL has recently been adapted, for example with the addition of fumarate, to alter the cross linking of the material to aid printing and alter the mechanical properties.[10] In the current study, methacrylate groups were added to the PCL to be suitable for Vat photopolymerization, leading to an optimized material for bone tissue engineering.

ELPs are recombinantly expressed polypeptides based on the properties of elastin and are highly biocompatible as these polypeptides are non-immunogenic.[11] The ELP matrix has been previously reported to sequester calcium and phosphate ions from the surrounding environment to nucleate apatite nanocrystals.[12] ELP matrix can also be applied as a coating on hard scaffolds to facilitate bone formation and osseointegration in vivo.[13] ELP can be mineralized in vitro to form hierarchical mineralized structures which can then promote bone formation, and this is a similar mechanism to that described by Wei et al. in the use of polycaprolactone to create lamellae which can "grow" in a saturated solution.[14] These lamellae were found to be biocompatible with positive in vitro and in vivo results when calcium and phosphate ions were within the scaffold structure.[15] The PEA, FN, and BMP-2 coating was developed to permit PEA to induce a fibrillar arrangement of FN, exposing FN binding sites to present BMP-2 to adjacent skeletal cells, enhancing osteogenic differentiation while utilizing low concentrations of BMP-2.[16] The nanoclay, Laponite, has been shown to sequester growth factors, such as vascular endothelial growth factor or BMP-2, allowing targeted delivery to the requisite site with a subsequent angiogenic or osteogenic tissue response induced.[8,17–19] It has been discovered that Laponite can be used to create gradients and patterns of bioactive proteins within the scaffold structure, to direct cell differentiation which may result in a more precise and temporal regulation of cell behavior during degradation of the Laponite.[20] Scaffolds of polycaprolactone have been engineered with graphene and graphene oxide to increase reactive oxygen species to target neoplastic cells.[21] With further research, Laponite could be used to sequester chemotherapeutic drugs for targeted, local delivery to cancer cells on a specially designed scaffold.

In our previous study, only the Laponite coating, when used to bind BMP-2, was effective at inducing robust ectopic bone formation and osteogenic differentiation in vitro.[8] Previous work however, indicated that the ELP and PEA/FN/BMP-2 coatings may function optimally in the osteogenic environment of an orthotopic site — such as in a model of fracture repair.[9,13,16,22] Therefore, application of all the coatings in a fracture model was performed to determine the efficacy of each coating in promoting bone repair. In these studies, we use an optimized preclinical critical-sized mouse femur defect model undertaking sequential data collection over the 8-week study period.

Critical-sized femur defects have been used in rodents to assess bone formation in a plethora of studies.[23] Thus, in mice, plates with screws, external skeletal fixators (ESFs), and variations in defect length from 2 to 4 mm depending on the type of mouse have been examined.[24–28] In studies of the fractured bone, fracture gaps of 0.1 to 2 mm were maintained by an ESF in the mouse femur, however, a defect of 3 mm is deemed necessary to be of critical size.[29,30] A femoral metaphyseal defect model in mice has been described in the examination of bone healing, although in the current work, such a defect model would have been too small to accept a solid 3D printed, porous scaffold.[31] Intramedullary (IM) pinning was the chosen method of stabilization of the scaffolds within the femur defect.[32] This was a refined method as the pin did not exit the femur proximally and distally, limiting injury to the mice and damage to the medullary canal, with the use of a shorter pin centrally within the scaffold, retaining the scaffold in place (Figure S1, Supporting Information).

In an initial pilot study, poly(caprolactone) scaffolds and collagen sponge loaded with BMP-2 as a positive control stabilized using a metal pin were trialed. The hypothesis was that the scaffolds would be of sufficient length (5 mm) that non-union of the fracture gap would result while the collagen sponge containing BMP-2 would unite the femur ends. These key points were established in a pilot study (Figures S2 and S3, Supporting Information). In a second pilot femur defect study, the use of PCL-TMA900 scaffolds, stabilized with a hypodermic needle (25G) or polyimide/plastic tubing in the medullary canal allowed assessment of the biocompatibility of the PCL-TMA900. In addition, the welfare, imaging and histological analysis benefits and potential complications of using a plastic pin in comparison to a metal pin were examined (Figure S4, Supporting Information). The radiolucent plastic pin was found to be suitable for IM fixation, microcomputed tomography (μCT) imaging and histological analysis, with, notably, negligible destruction of the animal tissues as pin removal was not required.

Thus, the current study has examined bone formation on coated PCL-TMA900 scaffolds in comparison to the uncoated PCL-TMA900 scaffold (negative control) to determine the efficacy of the coatings on bone formation, alongside BMP-2 soaked collagen sponge scaffold (positive control). The hypothesis under examination was that at least one of the coated (ELP, PEA/FN/BMP-2, ELP/PEA/FN/BMP-2, or Laponite/BMP-2) scaffolds would induce significantly greater bone formation in the defect site over

A. Hasan, A. Mata
School of Pharmacy
University of Nottingham
Nottingham NG7 2RD, UK
A. Mata
Department of Chemical and Environmental Engineering
NIHR Nottingham Biomedical Research Centre
University of Nottingham
Nottingham NG7 2RD, UK

© 2024 The Author(s). Advanced Materials Interfaces published by Wiley-VCH GmbH

21967350, 2025, 1, Downloaded from https://onlinelibrary.wiley.com/doi/10.1002/admi.202400389 by Imperial College London, Wiley Online Library on [17/01/2025]. See the Terms and Conditions (https://onlinelibrary.wiley.com/terms-and-conditions) on Wiley Online Library for rules of use; OA articles are governed by the applicable Creative Commons License

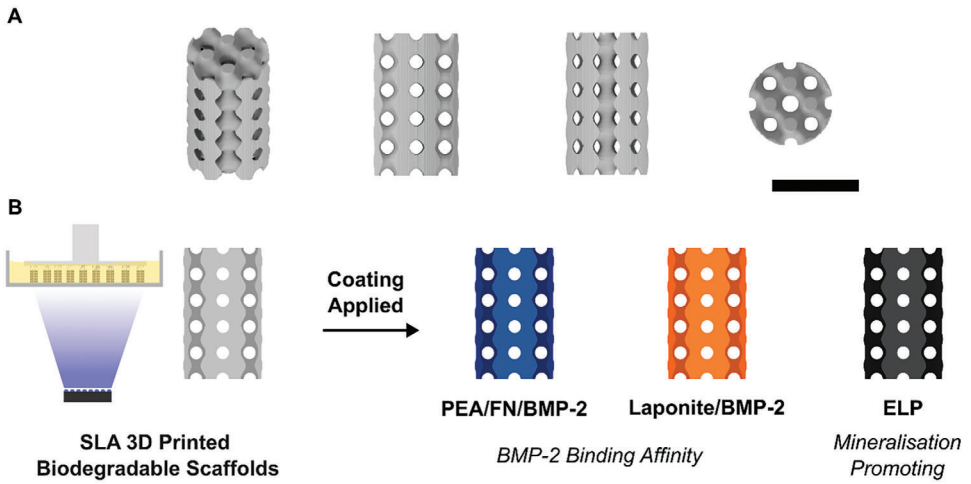


Figure 1. A) CAD model showing various views of the 3D printed scaffold. Height = 5 mm, diameter = 3 mm, central hole = 0.6 mm, pore size = 0.5 mm. Scale bar = 3 mm. B) The SLA printing process and osteogenic coating options are illustrated.

an 8-week period compared to the uncoated control, as assessed by μCT imaging and histology.

2. Results

2.1. Design of the 3D Printed PCL-TMA900 Scaffold

The scaffold shape was printable per the CAD model design, with multiple pores within the body of the scaffold and a central hole for the IM pin (**Figure 1**). The robust material was easy to handle and did not fragment during implantation.

2.2. Gross Dissection

The current studies aimed to assess the suitability of the PCL-TMA900 material with ELP, PEA/FN/BMP-2, ELP/PEA/FN/BMP-2 or Laponite/BMP-2 coating to promote bone formation in a murine femur defect model. The scaffolds were designed to fit within the critical murine femur defect, contained pores to enable good diffusion through the scaffold and a central channel to allow for a plastic pin at the proximal end of the distal femur fragment to avoid displacement of the scaffold (Figure S5, Supporting Information).

There were no signs of inflammation or infection around any of the constructs examined during the study. In mice with the PCL-TMA900 scaffolds implanted, limb movement was restricted in abduction and full retraction, however, the mice would not usually perform such movements when conscious, therefore this did not hinder normal activity or appear to cause discomfort. The scaffold was firmly held abutting the proximal femur; therefore, the distal edge of the scaffold was palpable and the distal femur adducted inwards, due to the pull of the quadriceps and contraction of the medial soft tissues. This caused an almost 90° bend in the plastic pin at the proximal end of the distal femur fragment (Figure S15, Supporting Information).

2.3. μCT Analysis of Bone Formation Within the Femur Segment and Scaffold Region

Initially on the day of surgery, the transected limbs were not aligned in all planes, as the pin was not tight within the marrow cavity allowing some pin movement. Due to a conservative approach adopted in the ostectomy surgery, the operative limb was longer than the contralateral limb initially as the bone fragment removed was smaller (approximately 3 mm in length) than the 5 mm long scaffold (Figure S16, Supporting Information). The distal limbs displayed a clear angulation at week 2 seen on μCT due to bending of the plastic pin at the proximal extent of the distal femur (**Figure 2**). The angulation of the femur at the distal end of the scaffold was not undertaken given the 3D geometry. Further analysis and data are provided in the Supporting Information.

The limbs were stable as the soft tissues contracted medially and thus the defect was not able to be manipulated or destabilized from week 2 onwards as observed while mice were anaesthetized for μCT image acquisition. The mice with ELP/PEA/FN/BMP-2 coated scaffolds displayed more aligned limbs, although the method of surgery was the same. Cranial angulation of the limb was apparent in the ELP/PEA/FN/BMP-2 coated scaffold group, rather than medial bending (Figure S17, Supporting Information). The collagen sponge and Laponite/BMP-2 coated scaffolds displayed a marked bone formation response from week 2 onwards with bone formation bridging the defect over the 8-week study (Figure S17, Supporting Information). The bone formed within a segment from the neck of femur to distal femur was quantified however, the medial angulation led to variation in bone formation (Figure S18, Supporting Information). The average bone volume of each group was comparable at the start of the study. At week 2, a marked increase in the bone volume of the collagen/BMP-2 group was observed. There was a subsequent reduction in volume of the collagen/BMP-2 group over the following 6 weeks. The remaining groups of ELP, PEA/FN/BMP-2, ELP/PEA/FN/BMP-2, and Laponite coated scaffolds displayed a temporal increase in bone volume to week 4 before a plateau was observed until week 8, with limited progression in bone

© 2024 The Author(s). Advanced Materials Interfaces published by Wiley-VCH GmbH

21967350, 2025, 1, Downloaded from https://onlinelibrary.wiley.com/doi/10.1002/admi.202400389 by Imperial College London, Wiley Online Library on [17/01/2025]. See the Terms and Conditions (https://onlinelibrary.wiley.com/terms-and-conditions) on Wiley Online Library for rules of use; OA articles are governed by the applicable Creative Commons License

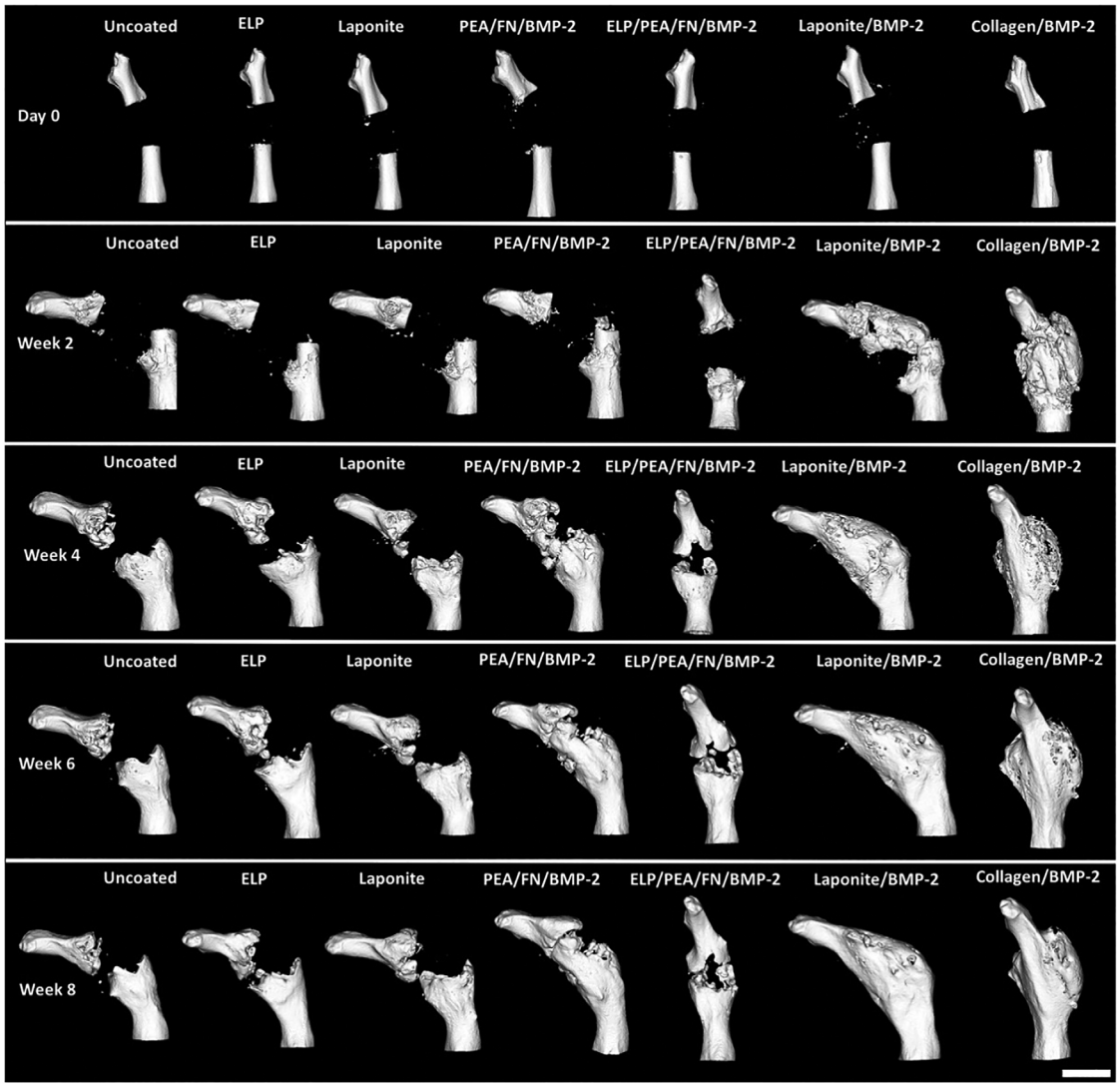


Figure 2. Cranial view of the femurs using μCT showing changes in bone volume observed over time. From the initial scans the pin bent and remained at the same angle from week 2 onwards. This resulted in an inward, medial bend to the limb in all mice except the ELP/PEA/FN/BMP-2 group. Over time the Laponite/BMP-2 coating displayed the greatest bone healing compared to the other coating groups. The collagen/BMP-2 group displayed complete union of the fracture site with smooth remodeling of the cortex craniomedially. Representative images shown from each group ($n = 6$, $n = 5$ for ELP/PEA/FN/BMP-2 after week 2), scale bar 5 mm.

formation, while the Laponite/BMP-2 scaffolds displayed some bone volume reduction between week 4 to week 8, perhaps due to remodeling (Figure S18, Supporting Information). On further analysis, the average bone volume for each group displayed a similar trend of bone formation to week 4 and no further obvious progression. The collagen/BMP-2 bone volume was observed to increase to week 2 followed by a decrease in bone volume, due to the dense bone formation around and within the collagen sponge perhaps leading to contraction of the sponge (Figure S19, Supporting Information). When analyzed as a percentage increase in bone volume, there was no significant difference between all the groups examined (Figure S20, Supporting Information).

At week 8, the μCT scans displayed union of the femur ends via the PCL-TMA900 scaffold in the Laponite/BMP-2 coated PCL-TMA900 scaffold group, and via a bulbous callous in the collagen sponge/BMP-2 group. There was no union of the femur ends observed in the ELP, Laponite, PEA/FN/BMP-2, ELP/PEA/FN/BMP-2 coated PCL-TMA900 scaffold groups and the uncoated scaffold served as the comparator with no obvious bone formation over or within the uncoated PCL-TMA900 scaffold (**Figure 3**).

The ex vivo μCT scans were comparable to the in vivo scans with the union of the fracture in the Laponite/BMP-2 and collagen sponge/BMP-2 groups only (Figure S21, Supporting Information).

Bone volume was analyzed using a 6 × 4 mm cylindrical volume around the defect site. A significant difference was found when comparing the uncoated PCL-TMA900 to the Laponite/BMP-2 and collagen/BMP-2 constructs, with an average of 8.2 mm^3 of new bone compared to 14.8 mm^3 and 14.0 mm^3

© 2024 The Author(s). Advanced Materials Interfaces published by Wiley-VCH GmbH

21967350, 2025, 1, Downloaded from https://onlinelibrary.wiley.com/doi/10.1002/admi.202400389 by Imperial College London, Wiley Online Library on [17/01/2025]. See the Terms and Conditions (https://onlinelibrary.wiley.com/terms-and-conditions) on Wiley Online Library for rules of use; OA articles are governed by the applicable Creative Commons License

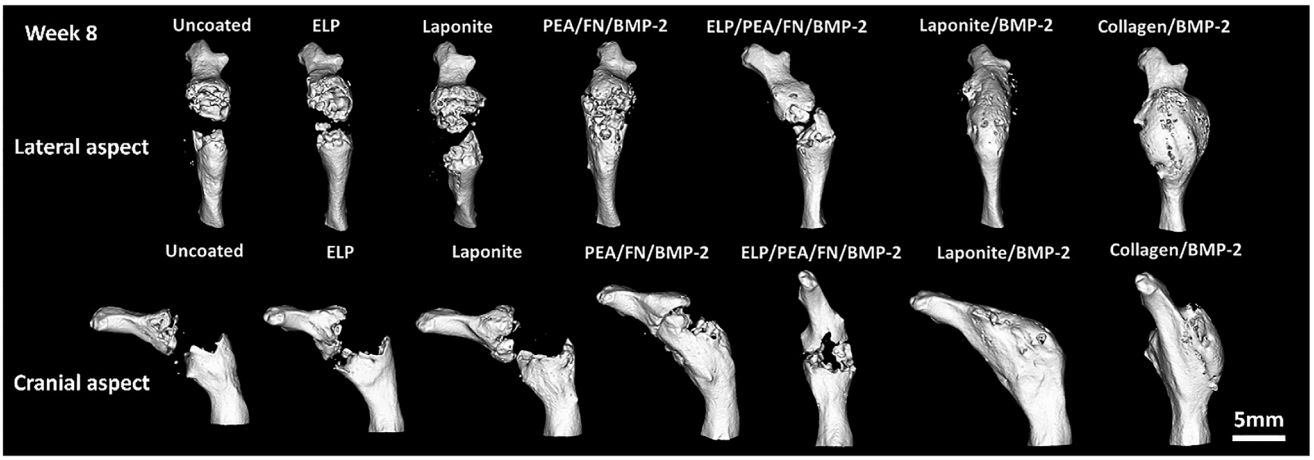


Figure 3. Representative μCT images from the lateral and cranial aspects of the limb with maximal bone formed in each group. Due to the pin bending, an inward, medial bend to the limb resulted in all mice except the ELP/PEA/FN/BMP-2 group. Over time the Laponite/BMP-2 coating displayed the largest bone healing compared to the other coating groups. The collagen/BMP-2 group displayed complete union of the fracture site with smooth remodeling of the cortex craniomedially and a spherical shell of bone laterally and caudally. Representative images shown from each group ($n = 6$, $n = 5$ for ELP/PEA/FN/BMP-2), scale bar 5 mm.

respectively (**Figure** 4A). Additionally, when analysis focused on the 3 × 5 mm cylindrical volume of the scaffold itself or collagen sponge constructs to determine the bone formed within the scaffold volume, there remained a significant difference between the uncoated PCL-TMA900 scaffold and the Laponite/BMP-2 and collagen/BMP-2 groups with 1.2 mm^3 of bone formed compared to 5.5 mm^3 on the Laponite/BMP-2 coated scaffold and 6.4 mm^3 in the collagen sponge/BMP-2 group (Figure 4B). Further, the medial and lateral aspects of the 3 × 5 mm cylindrical volume were analyzed demonstrating the Laponite/BMP-2 coated PCL-TMA900 scaffold contained significantly greater bone formation laterally than the PEA/FN/BMP-2 coated PCL-TMA900 scaffold (average of 1.1 mm^3 compared to 0.4 mm^3). There was no significant difference on the medial aspect between the three scaffold coating groups (Figure 4C).

2.4. Histology Demonstrated Intramembranous and Endochondral Ossification During Bone Formation

Histology of the limbs indicated distinct populations of cells within the tissues as the bone healing process progressed. The limbs selected for histology images were those with the greatest degree of bone formation on μCT results to enable bone formation analysis if present upon sectioning. The angulation of the limbs and scaffold within each defect can be seen (Figure S22, Supporting Information), with bone formation as per the μCT images. The bone shelf formed medially by intramembranous ossification from the periosteum which abutted the scaffold. Chondrocytes could be observed, illustrating endochondral ossification in action on the medial aspect of the limb. The lateral aspect of the uncoated scaffold was covered in fibrous tissue (**Figure** 5A). The ELP coated PCL-TMA900 scaffold displayed similar findings with new bone formation mostly medially and chondrocytes extending from this bone proximally along the medial aspect of the scaffold, extending toward the proximal extent of the femur (Figure 5B). This was likely due to the exaggerated angulation of the limb and biomechanics encouraging the medial bone to form more than on the lateral aspect of the limb. The Laponite only coated PCL-TMA900 scaffolds encouraged no bone to form along or within the scaffold, with only the bone tissue forming on the medial aspect of the limb, again likely due to the angulation and forces on the limb, similar to the uncoated and ELP only coated scaffolds, which also did not induce endochondral ossification or bone formation around or within the scaffold (Figure 5C). In the PEA/FN/BMP-2 coated PCL-TMA900 scaffold, the tissues had infiltrated into the pores of the scaffold and ossified, producing cortical type bone with regularly spaced osteocytes surrounding marrow cavities of cancellous type bone, which was vascularized, as evidenced by blood cells seen in the Goldner's trichrome stained sections (Figure 5D). Bone was observed to be formed predominantly medially and dorsally in this example mouse. The ELP/PEA/FN/BMP-2 coated scaffold had minimal bone formed in the center of the scaffold on μCT analysis although, bone tissue extending from proximally and distally around the periphery of the scaffold could be seen. The bone was mature cortical bone abutting fibrous tissue which extended into the pores of the scaffold, with chondrocytes gathered here as endochondral ossification was progressing (Figure 5E). The Laponite/BMP-2 coated PCL-TMA900 scaffolds showed the most pronounced and uniform new bone formation on μCT and this was confirmed upon histological staining. The periphery of the scaffold was encased in cortical bone with osteocytes within the matrix and areas of osteoid as the bone matured, while the pores of the scaffold were lined with cortical bone surrounding bone marrow, with blood cells seen within the marrow cavities (Figure 5F). The collagen sponge with BMP-2 formed smooth cortical bone craniomedially and a thin spherical shell caudolaterally which was seen by μCT and grossly upon dissection. The histology showed thicker cortical bone bridging the distal femur to proximal femur medially, with more fragile, less directionally orientated bone laterally, as noted on the μCT images (Figure 5G and Figure S22, Supporting Information). The bone formation over a representative scaffold in each group is shown in Figure S22 (Supporting Information).

 © 2024 The Author(s). Advanced Materials Interfaces published by Wiley-VCH GmbH

21967350, 2025, 1, Downloaded from https://onlinelibrary.wiley.com/doi/10.1002/admi.202400389 by Imperial College London, Wiley Online Library on [17/01/2025]. See the Terms and Conditions (https://onlinelibrary.wiley.com/terms-and-conditions) on Wiley Online Library for rules of use; OA articles are governed by the applicable Creative Commons License

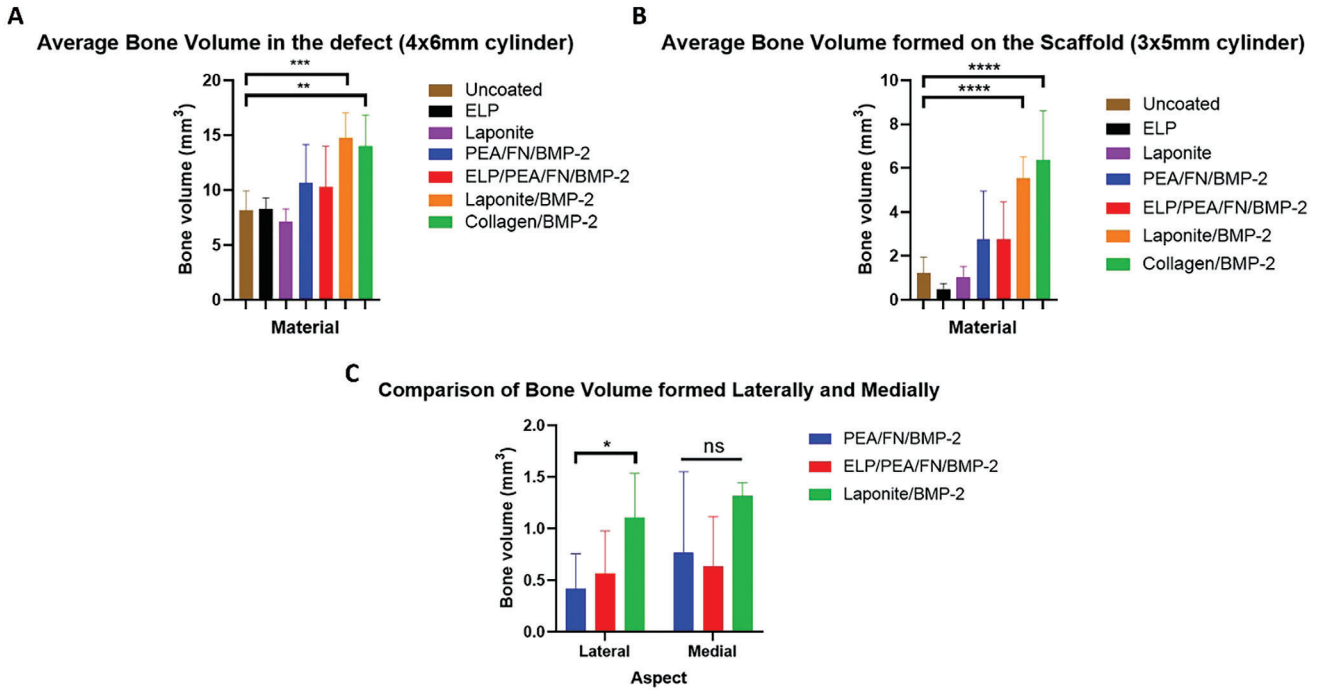


Figure 4. Quantification of bone volume using ex vivo images at week 8. A) The Laponite/BMP-2 and collagen sponge/BMP-2 constructs had significantly greater bone formation than the uncoated PCL-TMA900 scaffolds, $n = 6$ each group, except $n = 5$ for ELP/PEA/FN/BMP-2 group, one-way ANOVA with Dunnett's multiple comparisons test, $^{**}p < 0.01$, $^{***}p < 0.001$, mean and S.D. shown. B) Corroborating the findings in (A), only the Laponite/BMP-2 and collagen sponge/BMP-2 constructs displayed significantly greater bone formation than the uncoated PCL-TMA900 scaffolds, $n = 6$ each group, except $n = 5$ for ELP/PEA/FN/BMP-2 group, one-way ANOVA with Dunnett's multiple comparisons test, $^{****}p < 0.0001$, mean and S.D. shown. (C) A significant difference was found between the lateral aspect of the scaffold in Laponite/BMP-2 coated and PEA/FN/BMP-2 coated groups. There was no significant difference on the medial aspect of the scaffold between any of the 3 groups. $N = 6$ each group, except $n = 5$ for ELP/PEA/FN/BMP-2 group, 2-way ANOVA with Tukey's multiple comparisons test performed, ns, not significant, $^{*}p < 0.05$, mean and S.D. shown.

TRAP staining was used to visualize osteoclast location to assess regions of remodeling. The histology showed osteoclasts were active around the scaffold and at the proximal and distal bone ends. Osteoclasts were observed within the pores of the scaffolds and uniformly along the edge of the bone formed in the collagen sponge/BMP-2 group (**Figure 6**).

3. Discussion

The current study has examined bone augmentation, using functionalized (ELP, PEA/FN/BMP-2, ELP/PEA/FN/BMP-2, or Laponite/BMP-2) coated PCL-TMA900 scaffolds, with the hypothesized potential to induce skeletal cell differentiation. Laponite with BMP-2, as a coating on the PCL-TMA900 scaffold material, was successful in uniting the fracture with significant bone formation around and within the porous scaffold. Nonunion of the bone ends in mice with the uncoated PCL-TMA900 scaffold and bridging bone formation using the collagen sponge with BMP-2 (5 µg) was observed, confirming suitable scaffold length, scaffold material, and mass of BMP-2 applied to the positive control.

In the study, the Laponite/BMP-2 coated scaffolds were the only coated scaffold group to show a markedly significant difference from the uncoated PCL-TMA900 in bone volume formed over the 8-week study. Therefore, the hypothesis that coating a scaffold with an osteoinductive coating would significantly improve bone formation was confirmed as anticipated. The benefit of this coating compared to other methods of BMP-2 delivery is the significant reduction in BMP-2 required and the localization of the bone formation around the scaffold material. The Laponite/BMP-2 coating on PCL-TMA900 united the fractured bone ends and contained new bone at the periphery of the scaffold and within the scaffold pores, indicating adequate scaffold pore size with no surplus, ectopic bone formation in the surrounding soft tissues. The Laponite/BMP-2 coating was used immediately once dry as previous work has shown that a delay in use may affect efficacy.[8]

ELP coating on a solid scaffold material has been shown to enhance integration between the scaffold and bone but had not been found to significantly contribute to bone formation when compared to uncoated controls.[13] The PEA/FN/BMP-2 coating has previously been applied with successful bone formation in murine radial defects and veterinary clinical cases, when combined with autograft.[16,41] However, the PEA/FN/BMP-2 coating was not found to produce reliable, consistent bone volumes in this study, potentially as a consequence of the PEA/FN/BMP-2 coating relying on a greater surface area such as on porous granular materials to deliver a critical mass of BMP-2 to take advantage of the PEA/FN/BMP-2 reciprocal binding. The PEA coats the scaffold and therefore it can only hold a certain quantity of fibronectin, which in turn can bind to a certain mass of BMP-2. The use of granules with a large surface area would aid the total

© 2024 The Author(s). Advanced Materials Interfaces published by Wiley-VCH GmbH

21967350, 2025, 1, Downloaded from https://onlinelibrary.wiley.com/doi/10.1002/admi.202400389 by Imperial College London, Wiley Online Library on [17/01/2025]. See the Terms and Conditions (https://onlinelibrary.wiley.com/terms-and-conditions) on Wiley Online Library for rules of use; OA articles are governed by the applicable Creative Commons License

21967350, 2025, 1, Downloaded from https://onlinelibrary.wiley.com/doi/10.1002/admi.202400389 by Imperial College London, Wiley Online Library on [17/01/2025]. See the Terms and Conditions (https://onlinelibrary.wiley.com/terms-and-conditions) on Wiley Online Library for rules of use; OA articles are governed by the applicable Creative Commons License

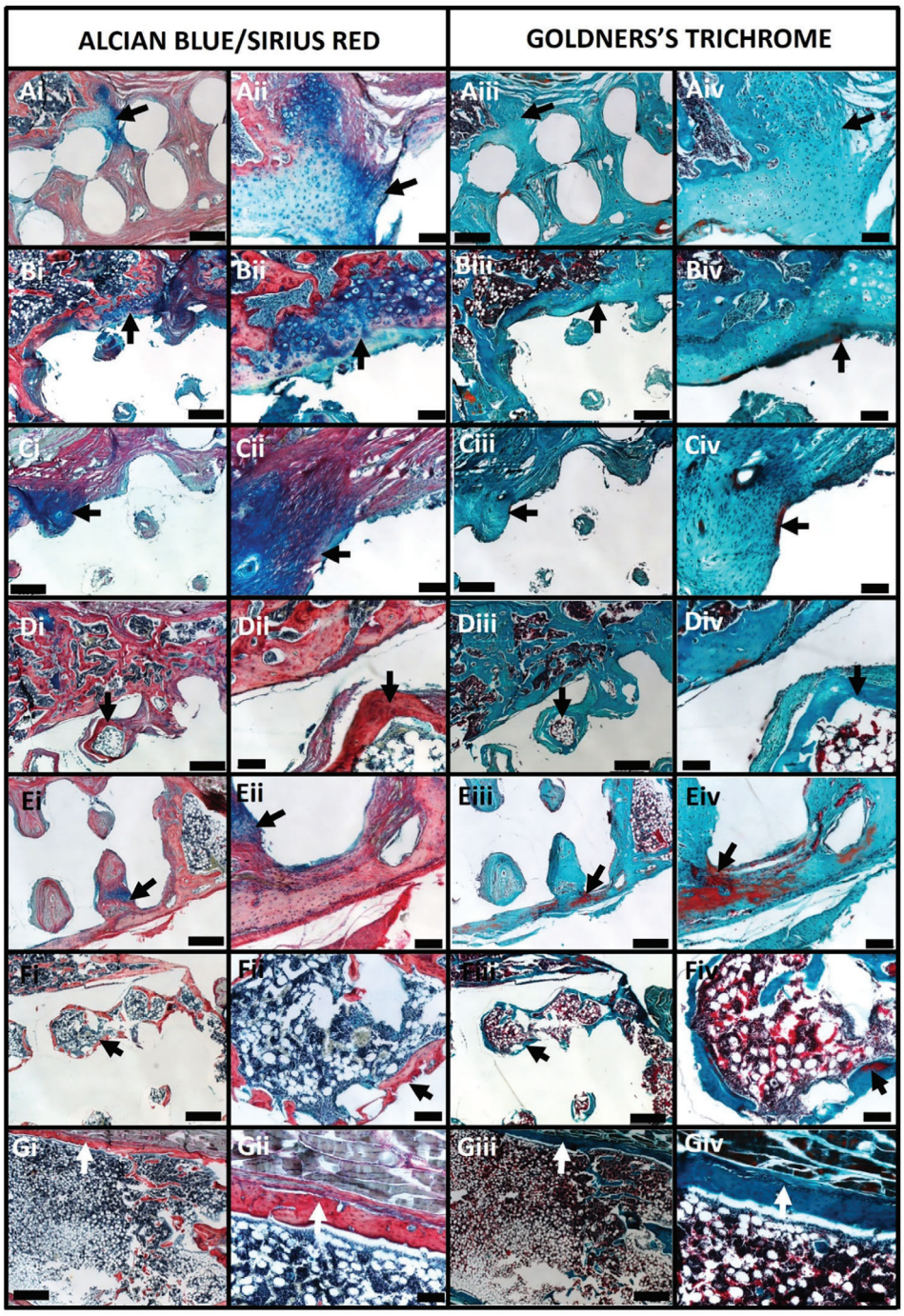


Figure 5. Histological analysis of bone formation surrounding the PCL-TMA900 scaffolds and collagen sponge/BMP-2 construct using Alcian Blue/Sirius Red (AB/SR) and Goldner's Trichrome (GT) staining. The medial aspect of the limb is to the top and lateral aspect to the bottom, proximal femur to the right and distal femur to the left of each image. A) Uncoated PCL-TMA900 scaffold: Ai, Aii) A population of chondrocytes in blue-staining proteoglycan matrix around the structure of the scaffold medially (black arrow). Aiii, Aiv) The medial new bone and a population of chondrocytes in within tissue surrounding the structure of the scaffold medially (black arrow). B) ELP coated PCL-TMA900 scaffold: Bi, Bii) The new bone medially and chondrocytes clusters (black arrow) at the junction between the new bone and the scaffold itself with fibrous tissue within the cylindrical pores of the scaffold. Biii, Biv) Osteoid tissue (black arrow) forming along the scaffold medially at the edge of the chondrocytes. C) Laponite coated PCL-TMA900 scaffold: Ci, Cii) Red fibrous collagenous tissue with a large area of blue proteoglycan matrix and chondrocytes on the medial aspect of the limb forming a thin area of bone matrix (black arrow). Ciii, Civ) Osteoid tissue (black arrow) surrounded by proteoglycan-rich matrix and cellular environment. D) PEA/FN/BMP-2 coated PCL-TMA900 scaffold: Di, Dii) The bone medially with islands of marrow cavity within a layer of cortical bone formed around the coated scaffold material. Bone tissue formed within the pores of the scaffold as cylindrical areas of cortical bone enclosing a central marrow cavity (black arrow). Diii, Div) The new mature cortical bone along the edge of a pore within the scaffold (black arrow). E) ELP/PEA/FN/BMP-2 coated PCL-TMA900 scaffold: Ei, Eii) Mature cortical bone with osteocytes embedded in the calcified matrix while fibrous tissue surrounded the scaffold and within the pores with

 © 2024 The Author(s). Advanced Materials Interfaces published by Wiley-VCH GmbH

mass of BMP-2 able to be delivered to the fracture site. The "critical mass" of BMP-2 to induce bone formation in rodents has been deemed as ≈1 µg of BMP-2, but a lower mass may be efficacious if sequestered in the bone fracture site to provide a consistent stimulus for osteogenic differentiation of skeletal cell populations.[19] Laponite's mechanism of action also relies on this principle of sequestering BMP-2 to provide bone formation using lower masses of BMP-2, reducing cost and potential adverse effects clinically.

This ability of Laponite to hold an active growth factor could be used for a variety of growth factors and ions which may induce osteogenesis, angiogenesis, or regeneration of other tissue types. The effect on angiogenesis and the immune system was not performed in this study, however, these are key components to determine prior to clinical applications and further work with tissues collected is possible. Xu et al. published on the material properties of hypoxia-mimetic hydrogels for tendon-to-bone healing.[42] Further, the group looked at the expression of markers of vascularization, cell differentiation, and effect on macrophage polarization.[42] Laponite could also be used to sequester antibacterial or immune stimulating factors in a combination approach to complicated bone injuries. Ongoing studies within our research groups are examining the uptake and processing of Laponite by macrophages and the subsequent in vivo biodistribution and clearance of Laponite. Macrophages immediately accumulate Laponite gels, and the elements of Laponite are subsequently excreted via the liver, kidney, spleen, and bladder (unpublished data). The use of ions such as copper alongside bioactive glass particles has been investigated as having triple benefits of anti-bacterial, osteogenic, and angiogenic properties.[43] Culture of the Laponite/antimicrobial coated scaffolds in a bacterial culture environment could give an indication of the ability to resist or combat surrounding infection.

Consistently, the lack of mineralization around the uncoated PCL in the first pilot study or PCL-TMA900 in the second pilot study and current study was unsurprising, given the absence of an osteogenic component on the scaffold surface to induce bone formation. This critically, highlights the requirement for an in vivo validated osteogenic component on 3D printed scaffolds to enhance their potential as biodegradable scaffolds for bone augmentation. The collagen sponge delivering 5 µg of BMP-2 was sufficient as a positive control. The bone bridging induced from the collagen sponge began some distance from the transected bone ends as the transected bone ends did not "regrow" themselves. BMP-2 can affect the periosteum and endosteum to recruit progenitor cells to differentiate toward chondrogenic or osteogenic lineages respectively.[44] Therefore, bone forms as an outer shell from the periphery of the sponge with the periosteum appearing to play a significant role in forming a bone shell by intramembranous ossification. To avoid overinterpretation and due to the scaffold shape and the bone formation being a dense covering over the scaffold, trabecular number and trabecular separation were not determined.

One mouse in the ELP/PEA/FN/BMP-2 coated group died on day 19 postoperatively due to a systemic, presumably anaerobic, bacterial infection. There were no signs of lameness, inflammation, or bone lysis present at the week 2 µCT analysis, therefore the infection was possibly unrelated to the study. At week 8, mouse 4 in the uncoated PCL-TMA900 group was noted to have two cavities within the proximal femur, likely due to pressure resorption due to the plastic pin against the bone, however, the final bone volume of the segment was comparable to the other five mice in this group and thus was included in the analysis of the femur segment volumes but regardless, the quantification of bone volume around the scaffold would not have been affected by this finding.

Previous reports describe stabilizing the fractured femur with an IM needle from the greater trochanter through the distal femur and stifle joint.[32,45,46] This published method ensured adequate stability of the fracture site and material held within the bone defect, however it was not conducive to sequential, quantitative radiographic imaging. Clough and colleagues inserted a metal pin via the transected bone ends with a metal spacer to maintain the gap in the bone, which was radiodense.[40] Removal of the metal spacer implant was described by sharp dissection prior to histology which would potentially damage the delicate forming tissue, while the use of a polyimide plastic pin negates this issue.[40] The IM pin insertion method chosen was to limit surgical trauma to the femur and prevent decimation of the entire bone marrow cavity. Consideration was given for thermal necrosis and osteoclastic activity at the bone ends due to the bone saw, however, this bone lysis was not observed to the same degree when the plastic pin was used compared to the metal pin, perhaps due to less stress shielding of the surrounding cortical bone. In the first pilot study using metal IM pinning, one mouse suffered a complication of displacement of the distal femur segment at week 8, likely due to the density of the pin protecting the scaffold and surrounding bone from stimulatory forces, leading to resorption of bone in the distal femur segment over the preceding weeks.

In the pilot studies, an attempt to ameliorate the scatter and beam hardening artefacts using a copper filter during µCT scanning was made, but there remained artefacts from the metal. Therefore, the quantification of bone volume when using the plastic pin was thought to be markedly more accurate, with reduction in human error compared to the necessity of manual selection of areas to disregard due to scatter from the metal pin, when using the analysis software.[40] The mice were scanned every 2 weeks to monitor bone formation over time. No detrimental effect on healing of the fracture callus has been found with sequential weekly µCT scans, and the inclusion of control mice allowed comparison of data generated.[47]

differentiation of chondrocytes potentially leading to further bone tissue formation (black arrow). Eiii, Eiv) The osteoid within the cortical bone (red arrow). F) Laponite/BMP-2 coated PCL-TMA900 scaffold: Fi, Fii) Cortical bone within the pores of the scaffold (black arrow) and marrow cavities within the pore spaces. Fiii, Fiv) The osteoid tissue (black arrow) formed, with extensive red blood cells seen within the marrow cavity enclosed by the new bone. G) Collagen/BMP-2 construct: Gi, Gii) The cranial aspect of the collagen sponge/BMP-2 construct showed the medial bone was uniform and over 100 µm thick in regions (white arrow) with a large marrow cavity formed within the bone shell. Giii, Giv) GT staining, with the cortical bone (white arrow) and vascular marrow cavity seen. (i and iii columns scale bar 500 µm, ii and iv columns scale bar 100 µm).

© 2024 The Author(s). Advanced Materials Interfaces published by Wiley-VCH GmbH

21967350, 2025, 1, Downloaded from https://onlinelibrary.wiley.com/doi/10.1002/admi.202400389 by Imperial College London, Wiley Online Library on [17/01/2025]. See the Terms and Conditions (https://onlinelibrary.wiley.com/terms-and-conditions) on Wiley Online Library for rules of use; OA articles are governed by the applicable Creative Commons License

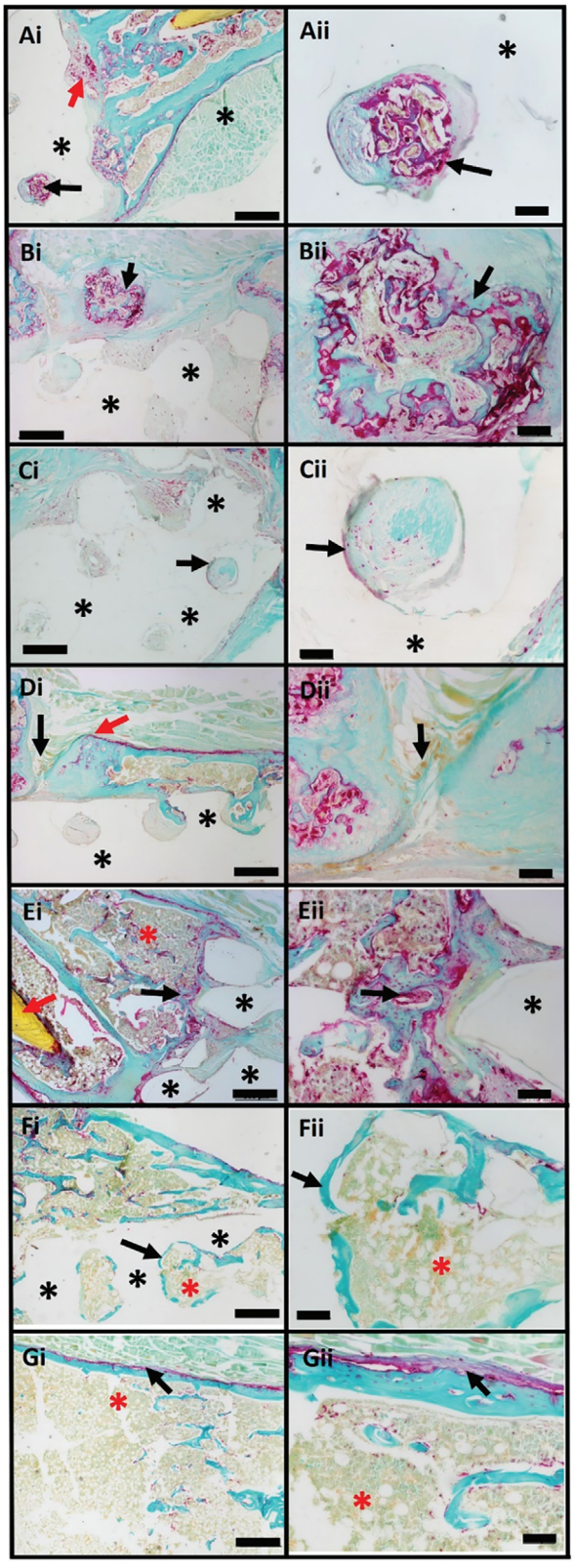


Figure 6. TRAP staining of histological sections to visualize regions of osteoclast activity. Ai, Aii) Uncoated scaffold; osteoclasts at the junction between the scaffold (*) and proximal end of the femur (red arrow) and within a pore of the scaffold (black arrow). Bi, Bii) ELP coated scaffold; osteoclasts (black arrow) around a mass of bone on the medial aspect of the limb adjacent to the scaffold (*). Ci, Cii) Laponite coated scaffold; relatively fewer osteoclasts were seen around the scaffold (*), with some within the pores of the scaffold. Di, Dii) PEA/FN/BMP-2 coated scaffold; osteoclasts (red arrow) lining the medial bone surface over the scaffold (*), and an area where bone from the proximal and distal femur has almost united (black arrow). Ei, Eii) ELP/PEA/FN/BMP-2 coated scaffold; osteoclasts at the junction between the new bone and the scaffold (*) (black arrow), with new bone formed by intramembranous ossification from the periosteum seen (red asterix) and the plastic pin (red arrow) seen within the section. Fi, Fii) Laponite/BMP-2 coated scaffold; quiescent cortical bone (black arrow) and mature marrow cavities (red asterix) formed within the pores of the scaffold material (*), with less osteoclast staining seen. Gi, Gii) Collagen/BMP-2; osteoclasts (black arrow) lining the new cortical bone around the marrow cavity (red asterix) formed by the collagen sponge/BMP-2 construct. (Left column scale bar 500 μm and right column scale bar 100 μm).

The plastic pin could be used to stabilize the bone ends and alleviate difficulties in μCT imaging and histology associated with use of metal stabilization. Results showed that the plastic pin was successful in holding the scaffold in position between the bone ends, permitted normal locomotion despite bending, could be imaged by μCT, and sectioned for histological analysis.

The PCL-TMA900 scaffolds and plastic pin were amenable to processing and sectioning during histological evaluation of bone formation. The histology by Kaur et al. mirrors the findings of the current studies with intramembranous bone formation between the periosteum and cortex of the transected bone ends.[48] It was found that the compressive strain medially promoted the formation of cartilaginous tissue, promoted by the cells at the edge of the transected end of the femur.[49] The tensile strains laterally induced the formation of fibrous tissue across the scaffolds, however, the Laponite/BMP-2 and collagen/BMP-2 constructs had mature mineralized bone both medially and laterally surrounding each construct, as the scaffold delivery of BMP-2 induced bone formation equally around the scaffold while this did not occur in the other scaffold coating groups.[50] The TRAP staining was used to indicate osteoclast activity around the scaffolds and within the pores of the scaffolds in each group. The Laponite and Laponite/BMP-2 groups appeared to have less osteoclast activity within the pores of the scaffold. Mature bone with marrow cavities were observed within the scaffold construct of the Laponite-BMP-2 group, while in contrast only collagenous tissue was observed in the Laponite only coated scaffold.

The mice had no rigid fixation of the scaffold within the fracture defect and could weight bear immediately postoperatively. The plastic pin fixation method was unstable initially with potential movement at the scaffold/bone end interface, but the soft tissues held the scaffold firmly between the bone ends by week 2. It is likely micromotion induced healing by endochondral ossification, with significant numbers of chondrocytes seen in histological sections around the distal bone end medially and on the periphery of the scaffold. The strain upon the fracture fragments, or in this case the scaffold and transected femur, was found to support healing. It would be interesting to examine different strain levels in future studies. Positive correlations have been found between fracture activity in the early

© 2024 The Author(s). Advanced Materials Interfaces published by Wiley-VCH GmbH

21967350, 2025, 1, Downloaded from https://onlinelibrary.wiley.com/doi/10.1002/admi.202400389 by Imperial College London, Wiley Online Library on [17/01/2025]. See the Terms and Conditions (https://onlinelibrary.wiley.com/terms-and-conditions) on Wiley Online Library for rules of use; OA articles are governed by the applicable Creative Commons License

postoperative 1–2 week period with low strain leading to direct primary healing, moderate strain leading to secondary healing via callus formation, with the motion reducing as healing progresses.[51] However, too large a strain leads to cessation of healing and nonunion of the fragments/construct and implant failure.[51,52] Conversely, if the fixation method is too rigid, healing will be abated leading to the indication that there is an optimal strain in a fracture site to initiate and propagate healing.[50] Cyclic compression has been found to lead to RUNX2 and BMP-2 production or increased sensitivity to BMP-2 in cells, leading to osteogenic differentiation.[53] The current model shows inverse dynamization, that is the flexible fixation becomes more rigid in the first 2 weeks in that as the limbs curved, the scaffolds prevented movement of the distal femur, leading to a more stable environment for further healing.[54] The stress or load would have been applied in the mice by weight bearing, especially when standing on their hindlimbs or through muscle contraction.[50]

Poly(caprolactone) trimethacrylate (PCL-TMA900) was chosen as a material which would biodegrade due to the presence of ester bonds and because of the material properties suitable for SLA 3D printing (i.e., lower glass transition temperature). The molecular weight was chosen as a compromise between suitable material properties (i.e., toughness and stiffness), while having a viscosity suitable for 3D printing. In an ideal situation, the 3D printed scaffold material would degrade on a timescale shortly after the formation of new bone in and around the scaffold, to allow for complete healing of the defect. While this is not the case within the present study as the scaffolds are still present after 8 weeks, due to their chemical composition, it would be expected that the scaffolds would degrade on a larger time scale (i.e., months to years). The complex environment into which the scaffolds are implanted makes correlation of in vitro degradation or accelerated degradation conditions to in vivo degradation challenging. Ultimately, longer follow up studies would be required to verify and tailor the degradation times. Crucially, we have demonstrated that the 3D printed PCL-TMA900 scaffolds show excellent biocompatibility and can support the formation of new bone with a suitable osteogenic coating. The nanotopography of the material was not enhanced in any way, with the shape of the scaffold creating ridges and grooves which may enhance cell and tissue attachment. In the recent literature, polycaprolactone-based scaffolds have been created with anisotropic micropores and nanotopographical patterns due to the extraction of polyethylene oxide from the mixture.[14] Further, the scaffolds were acellular and there was no decellularization steps involved in the manufacture of the scaffolds, thereby limiting the risk of immunogenicity and improving the rate of manufacture and use of the scaffold material. Laponite and PCL have been combined with decellularized extracellular matrix to create a membrane for bone repair with positive in vivo results, however, our aim was to produce an osteogenic, robust scaffold for limb bone defect repair.[55]

Due to the significant bone formation surrounding the Laponite/BMP-2 coated PCL-TMA900 scaffolds uniting the bone ends in this study, further studies with Laponite/BMP-2 coating in the ovine femoral condyle defect model were warranted to scale up the Laponite/BMP-2 coated construct to assess repeated efficacy of the Laponite/BMP-2 coating on PCL-TMA900 scaffolds prior to clinical translation.

4. Conclusion

This study used a novel murine femur bone defect method to confirm the biocompatibility and efficacy of bioactive coatings on rigid PCL-TMA900 polymer scaffolds for bone repair. The Laponite/BMP-2 coating induced solid union of the fracture due to significant mature bone formation on and within the PCL-TMA900 scaffold as seen by sequential μCT imaging and histology. The average bone volume formed within the scaffold area was over four times that when an uncoated scaffold was used (5.5 mm^3 compared to 1.2 mm^3). Bone formation on the Laponite/BMP-2 scaffold did not appear to rely on external forces, with similar bone formation medially and laterally around and within the scaffold. This was in comparison to the other coated scaffolds in which a significant difference (over twice as much bone formation) was seen on the lateral aspect of the limb in the Laponite/BMP-2 group compared to the PEA/FN/BMP-2 coated group. However, this study did not allow time for degradation of the scaffold material leading to a plateau of bone formation in each group, therefore, longer term studies should be considered. Further, the flexibility of the IM pin did not allow natural forces to be conferred upon the scaffold materials. This Laponite/BMP-2 coating on PCL-TMA900 scaffolds has been taken forward in an ovine femoral condyle defect model, to investigate the ability of the BMP-2 to induce bone formation when the scaffold shape is developed with an increase in magnitude of the bone defect in a critical-sized ovine metaphyseal bone defect.[56] The ovine model provided a necessary test of osteogenic efficacy and scaffold material stability on the path toward clinical application of the Laponite/BMP-2 coated PCL-TMA900 material for bone repair.

5. Experimental Section

Materials: Reagents were purchased as follows: Ethyl acrylate (E9706, Sigma, UK), ELP with statherin sequence (SN_A15) (Technical Proteins Nanobiotechnology, Valladolid, Spain); recombinant human BMP-2 (Infuse/InductOS Bone graft kit, Medtronic, USA); recombinant human fibronectin (R&D systems, Biotechne, UK); Laponite (BYK); phosphate buffered saline (PBS) (Scientific Laboratory Supplies, SLS); Alcian blue 8X, Light green SF, Orange G 85% pure, paraformaldehyde 96% extra pure, phosphomolybdic acid hydrate 80% (Acros Organics); Picrosirius Red, Van Gieson's stain, Weigert's Haematoxylin Parts 1 and 2 (Clintech Ltd, UK); acetone, acid fushsin, histowax, ponceau xylidine, silver nitrate, sodium hydroxide pellets, sucrose, glycine, l-glutamic acid, sodium chloride, polysorbate 80 (Merck, UK); dibutyl phthalate xylene (DPX), Histoclear (Thermofisher Scientific, UK); Fast green and sodium thiosulphate (VWR); Lubrithal (Dechra, UK), Isoflurane (Dechra, UK), Buprenorphine (Buprecare multidose, Animalcare, UK), and Vetasept sourced from MWI animal health, UK. 5/0 PDS II suture (Ethicon, USA) from NHS supply chain. All other consumables and reagents were purchased from Sigma-Aldrich, UK.

Scaffold Material Choice: Our research groups were interested in developing a bioresorbable stereolithography (SLA) 3D printable resin. SLA based 3D printing techniques using masked SLA or digital light projection (DLP) can be scaled appropriately for translational applications given the whole print bed can be utilized and scaled to decrease fabrication times which limit extrusion-based 3D printing approaches. Commonly, medical devices used clinically utilize poly(ester) derivatives such as poly(caprolactone), poly(lactic acid), poly(glycolic acid), and copolymers thereof which can degrade hydrolytically and enzymatically into oligomers which are bioresorbed. To make the polymers suitable for

© 2024 The Author(s). Advanced Materials Interfaces published by Wiley-VCH GmbH

21967350, 2025, 1, Downloaded from https://onlinelibrary.wiley.com/doi/10.1002/admi.202400389 by Imperial College London, Wiley Online Library on [17/01/2025]. See the Terms and Conditions (https://onlinelibrary.wiley.com/terms-and-conditions) on Wiley Online Library for rules of use; OA articles are governed by the applicable Creative Commons License

21967350, 2025, 1, Downloaded from https://onlinelibrary.wiley.com/doi/10.1002/admi.202400389 by Imperial College London, Wiley Online Library on [17/01/2025]. See the Terms and Conditions (https://onlinelibrary.wiley.com/terms-and-conditions) on Wiley Online Library for rules of use; OA articles are governed by the applicable Creative Commons License

SLA 3D printing, the polymers must contain photoreactive groups which initiate cross-linking of a liquid precursor to a solid material. Derivatives of poly(caprolactone) and poly(trimethylene carbonate) containing (meth)acryloyl functional groups are well suited for this purpose as the polymers have low glass transition temperatures, providing a liquid polymer which can be printed solvent free. This material property improves translatability and increases printing speed. While these polymers have been reported and their material properties characterized previously in the literature, an assessment of their biocompatibility and suitability as bioresorbable scaffolds for bone tissue engineering using large animal preclinical models has not been assessed.[33–37]

We have shown that a poly(caprolactone) trimethacrylate (PCL-TMA) with a degree of polymerizations (D_p) = 3, coated with various validated osteoinductive coatings did not show ectopic bone formation in a subcutaneous murine model despite displaying good biocompatibility in vitro and in vivo.[9] Continuing from this work, we changed the D_p of the poly(caprolactone) from 3 to 6 to increase the toughness of the scaffold. While the PCL-TMA resin from the first study had a higher Young's modulus due to the higher cross-linking density, this made the scaffold brittle and impractical for in vivo implantation in a bone tissue engineering context. Increasing the D_p of the poly(caprolactone) to 6 increased the toughness to improve workability of the scaffold, while still affording a suitable viscosity for SLA 3D printing. We demonstrated that a poly(caprolactone) trimethacrylate resin (PCL-TMA900) with a degree of polymerization (D_p) = 6, with a Laponite/BMP-2 coating demonstrated significant formation of ectopic bone when tested in a subcutaneous murine model and had comparable biocompatibility to the PCL-TMA resin.[8]

Synthesis of the PCL-TMA900 Polymer: PCL-TMA of this molecular weight has been synthesized and 3D printed using mSLA as previously detailed.[34,35,37] The PCL-TMA900 polymer was synthesized and characterized as detailed in Marshall et al.[8] using poly(caprolactone) triol, M_n = 830 Da as a starting material (Boc Sciences). Poly(caprolactone) triol (100 g, 0.12 mmol, 1 eq), anhydrous dichloromethane (300 mL), and triethylamine (100 mL, 0.72 mmol, 6 eq) were added to a 1 L two-necked round bottom flask. The reaction was placed under a nitrogen atmosphere and then cooled in an ice-water bath for 15 min. A pressure-equalizing dropper funnel charged with methacryloyl chloride (53 mL, 0.67 mmol, 4 eq) was attached to the round bottom flask. The methacryloyl chloride was added dropwise over approximately 3 h. The reaction was covered with aluminum foil to protect it from light and allowed to stir and warm to room temperature (RT) overnight. The next day, methanol (50 mL) was added to quench the reaction, which was allowed to stir at RT for 30 min. The reaction mixture was dissolved in dichloromethane (800 mL), transferred to a separating funnel and washed with 1 m aqueous hydrochloric acid solution (5 × 250 mL), saturated sodium bicarbonate solution (4 × 400 mL), and brine (1 × 400 mL). The organic layer was then dried with anhydrous magnesium sulphate, filtered and concentrated via rotary evaporation. The crude yellow liquid was then purified using a silica plug, with dichloromethane as the eluent. Fractions containing PCL-trimethacrylate were pooled and concentrated via rotary evaporation. The PCL-trimethacrylate was transferred to a brown glass vial and dried using a stream of air (through a plug of $CaCl_2$) overnight to yield the title compound as a slightly yellow viscous liquid (94.25 g). The PCL-trimethacrylate was supplemented with 200 ppm (w/w) of 4-methoxyphenol (MEHQ) as an inhibitor.

^{1}H NMR (400 MHz, $CDCl_3$) δ 6.11 – 6.05 (m, 3H), 5.61 – 5.50 (m, 3H), 4.16 – 3.99 (m, 18H), 2.34-2.27 (m, 12H), 1.96 – 1.88 (m, 9H), 1.71 – 1.60 (m, 26H), 1.47 – 1.31 (m, 12H), 0.98 – 0.83 (m, 3H).

The characterization data agrees well with that previously reported.[35] The degree of functionalization was determined as >90%.[8]

Scaffold Design and 3D Printing of the PCL-TMA900 Scaffolds: The poly(caprolactone) trimethacrylate (PCL-TMA900) scaffolds were designed using a custom Matlab script, based on the Schwarz P triply periodic minimal surface.[38] This resulted in a bicontinuous, porous, tubular shape (3 mm diameter, 5 mm height, pore size 0.5 mm and surface area 113.9 mm^2), with a central hole of 0.6 mm diameter for the IM pin.

The PCL-TMA900 scaffolds were printed using masked SLA 3D printing on a Prusa SL1S. The resin was prepared for 3D printing by initially dissolving 0.1% (w/w) 2,5-thiophenediylbis(5-tert-butyl-1,3-benzoxazole) (OB+) as a photoabsorber in the PCL trimethacrylate by stirring at RT for 1 h. Finally, 1.0% (w/w) diphenyl(2,4,6-trimethylbenzoyl)phosphine oxide (TPO-L) as a photoinitiator was added to the resin. The scaffolds were sliced in PrusaSlicer with their longitudinal axis parallel to the surface of the build platform. Supports and pads were used to raise the objects off the build platform, with 10 supports placed along the scaffold to ensure adhesion to the build platform during the printing while not compromising the structure. The scaffolds were sliced at a layer height of 50 µm using a 25 s exposure time per layer.

After printing, the scaffolds were rinsed with ethanol and removed from the build plate. The support structures were removed from the scaffolds with a fine sprue cutter, then the scaffolds were sonicated in ethanol (5 × 5 min) and allowed to dry for 15 min at RT. The scaffolds were postcured using a Formlabs Form Cure for 60 min at RT. After postcuring, the central hole of the scaffolds was cleared by hand with a 0.6 mm drill bit and rotation motion to ensure good fit with the pins. The scaffolds were then soaked in ethanol overnight at RT on a rocker (100 rpm), washed with ethanol (3×), and allowed to dry at RT before being ELP and/or PEA coated then sterilized by ethylene oxide (EO), or left uncoated and EO sterilized as the uncoated scaffold control group.

Intramedullary Pin Preparation: EO sterile, 1.2 cm long polyimide tubing (internal diameter 0.0136″, outer diameter 0.0231″, wall thickness 0.00475″, Microlumen, USA) was used as the IM pin in every mouse (Figure S1, Supporting Information). Initially, a metal pin was applied in the first pilot study, however, the metal pin produced µCT imaging artefacts, stress shielding, and bone resorption (Figures S2 and S3, Supporting Information). The polyimide/plastic pin was verified as suitable for use by implantation into cadaver mice and findings in the second pilot study which compared the use of a metal in contrast to a polyimide pin. Results showed that the plastic pin maintained the scaffold in position between the bone ends, with locomotion unaffected and could be imaged by µCT, and sectioned for histological analysis. Greater bone formation in the plastic IM pin group compared to the metal IM pin was found, however, this result was not statistically significant (Figure S4, Supporting Information). Furthermore, the biocompatibility of the PCL-TMA900 material scaffolds, was observed, with no adverse effects noted on gross or histological examination, similar to a previous subcutaneous implantation study.[8]

Preparation of the Uncoated and Coated PCL-TMA900 Scaffolds: The following scaffolds were prepared: a negative control group of uncoated PCL-TMA900 scaffolds (n = 6), together with ELP, PEA/FN/BMP-2, ELP/PEA/FN/BMP-2, Laponite alone or Laponite/BMP-2 coated PCL-TMA900 scaffolds (n = 7 scaffolds prepared for each group including a spare scaffold). The scaffolds were sterilized by EO prior to use as uncoated scaffolds, prior to the application of Laponite or after PEA or ELP coating. Prior to use, a 0.6 mm drill bit (KATUR, Amazon website) was autoclaved at 126 °C and inserted by hand, with rotation, into the central hole of each scaffold to ensure easy insertion of the polyimide tubing. In a class 2 hood, the scaffolds were threaded onto the polyimide tubing by hand wearing sterile nitrile gloves and placed in a 6-well plate to maintain sterility.

Preparation of the Uncoated and Coated PCL-TMA900 Scaffolds—PEA Coating Application: PEA coating of the scaffolds was performed using a custom-built plasma chamber as previously described.[39] In brief, the scaffolds were treated in air plasma for 5 min before being exposed to monomer plasma. Plasma polymerization of the ethyl acrylate monomer was carried out in a custom-made capacitively coupled plasma installation for low-pressure plasma in a 15-L T-shaped reactor made of borosilicate and stainless-steel end plates sealed with Viton O-rings. A vacuum was produced by a rotary pump or a scroll pump (both BOC Edwards, UK), with operating experiment pressures for the monomer plasma from 0.15 to 0.25 mbar. The plasma was initiated using two capacitively coupled copper band ring electrodes situated outside of the reactor chamber and connected to a radio frequency power supply (Coaxial Power System Ltd.) at 50 W for 15 min. The monomer pressure was controlled using speedivalves (BOC Edwards, UK) and monitored with a pirani gauge (Kurt J. Lesker).

Preparation of the Uncoated and Coated PCL-TMA900 Scaffolds—ELP Coating Application: ELP coating of scaffolds was based on previous

© 2024 The Author(s). Advanced Materials Interfaces published by Wiley-VCH GmbH

published methods.[13] In brief, lyophilized ELP powder was dissolved in a solvent mixture of DMF/DMSO (at 9/1 ratio, v/v) to prepare a 5% (w/v) ELP solution followed by addition of hexamethyl diisocyanate (HDI) crosslinker (cross-linker to lysine ratios of 12/1). 3D printed PCL-TMA900 scaffolds were immersed in the ELP solution for 10–15 s and left to dry overnight at RT (22 °C) within a glovebox (BELLE Technology, UK) maintained at a humidity <20%. Dry ELP coated scaffolds were subsequently washed several times with deionized water (dH_2O) to remove excess HDI and termed as ELP coated scaffolds.[13] The ELP coating was confirmed to be present on the PCL-TMA900 scaffold surface using scanning electron microscopy.[13] For the ELP/PEA/FN/BMP-2 coated scaffolds, the ELP coating was applied as described above, followed by PEA. Finally, the FN and BMP-2 were adhered to the scaffolds as described below.

Preparation of the Uncoated and Coated PCL-TMA900 Scaffolds—Application of FN and BMP-2 to the PEA Coating: The method of coating has been described in Marshall et al.[9] In brief, on the day of surgery, the PEA and ELP/PEA coated scaffolds were immersed in FN (20 µg mL^{-1}) followed by InductOs BMP-2 (5 µg mL^{-1}) with 1 scaffold per vacutainer and 1 mL of solution used per vacutainer using PBS (with $CaCl_2$ and $MgCl_2$) as the diluent, under vacuum for 1 h at RT. The scaffolds were rinsed in PBS with $CaCl_2$ and $MgCl_2$ and moved to a new vacutainer between FN and BMP-2 adsorption. The scaffolds were given a final rinse in PBS (with $CaCl_2$ and $MgCl_2$) before threading onto the polyimide tubing. The scaffolds were then placed in a sterile 6-well plate for transport to the animal research facility, as the FN/BMP-2 coating was bound to the scaffold material, therefore, critically, transfer of the coating to the surrounding surface was not a concern.

Preparation of the Uncoated and Coated PCL-TMA900 Scaffolds—Laponite and BMP-2 Coating: The method of coating has been described in Marshall et al.[8] In brief, a 1% (wt/wt) Laponite solution was prepared and stored at 4 °C, 48 h prior to use. An amount of 0.2 g Laponite was dispersed, under stirring in 19.8 g dH_2O and the resulting clear suspension autoclaved to sterilize. After autoclaving, the weight of lost dH_2O was replaced with sterile dH_2O. On the day of surgery, 14 PCL-TMA900 scaffolds were immersed individually in 1 mL of 1% (w/w) Laponite solution. After 1 h at RT in the sterile class II hood, the scaffolds were removed with sterile forceps and threaded onto 25-gauge needles in a 24-well plate (Figure S5, Supporting Information) facing upwards to ensure the scaffolds dried without risk of transfer of coating from the scaffold. The excess Laponite was gently removed with a 100 µL pipette tip. The scaffolds were allowed to dry for 2 h prior to use as a Laponite only coated scaffold ($n = 7$) or underwent further coating in BMP-2 ($n = 7$).

For BMP-2 binding, seven Laponite coated PCL-TMA900 scaffolds were immersed individually in 1 mL of 5 µg mL^{-1} BMP-2 (InductOs BMP-2) in PBS (not containing $CaCl_2$ and $MgCl_2$) in 1.5 mL low protein bind Eppendorf tubes at RT for 24 h. After 24 h, the PCL-TMA900 scaffolds were taken out of the BMP-2 solution and dried on needles in a category II hood. Polyimide tubing was threaded through the central hole of the scaffold prior to implantation.

Preparation of the Uncoated and Coated PCL-TMA900 Scaffolds—Collagen Sponge/BMP-2 Construct: Collagen sponges loaded with 5 µg of InductOs BMP-2 was used as the positive control scaffold. The collagen sponge was EO sterile but to ensure sterility, the collagen sponge was UV sterilized overnight in a sterile class 2 hood. Approximately 20, 3 mm × 3 mm collagen sponge pieces were threaded onto a 23-gauge needle. The BMP-2 was diluted with InductOs buffer (Table S1) to 333.33 µg mL^{-1} concentration and 15 µL of solution (5 µg mass of BMP-2) was added to the collagen sponge. With fluid addition, the collagen was molded into a single 5 mm length construct. The construct was then dried for 2 h to form a rigid 5 mm long scaffold and was then transferred from the needle to the polyimide tubing. The drying process did not denature the BMP-2 as shown in the pilot experiments and prevented the construct collapsing as much as if implanted when wet.

Mouse Type and Housing: All procedures were performed in accordance with University of Southampton institutional guidelines, with ethical approval from the Animal Welfare and Ethics Review Board and under UK Home Office PPL P96B16FBD and PPL PP8873619, in accordance with the regulations in the Animals (Scientific Procedures) Act 1986 and using the ARRIVE guidelines. Forty-two, adult, male, MF-1, wild-type mice, bred on site and group housed in individually ventilated cages (IVCs) were used. Mice had access to ad libitum standard pellets and water. All mice were healthy with similar mean weight per group (mean and standard deviations to 1 decimal place of weight for each group were: uncoated scaffold 49.9 ± 4.1 g, ELP coated scaffold 49.9 ± 6.3 g, PEA/FN/BMP-2 coated scaffold 49.6 ± 5.1 g, ELP/PEA/FN/BMP-2 coated scaffold 50.2 ± 8.7 g, Laponite coated scaffold 52.2 ± 3.6 g, Laponite/BMP-2 coated scaffold 49.2 ± 7.4 g, collagen sponge/BMP-2 construct 51.0 ± 7.1 g), with normal mobility prior to surgery.

Surgical Procedure: General anesthesia was induced in mice with an induction chamber using Isoflurane (5%) and 100% oxygen (0.8 L min^{-1} flow rate). The mouse was moved to the nose cone for maintenance of a surgical plane of anesthesia at approximately 2-2.5% isoflurane and 100% oxygen (0.8 L min^{-1} flow rate). Lubrithal (Dechra, UK) was applied to the eyes, ear marking was performed for identification, the entire left hindlimb and side to mid-body of the mouse was shaved, and chlorhexidine/alcohol solution applied. Buprenorphine (0.05 mg kg^{-1}) was administered by subcutaneous injection. In right lateral recumbency, the left hindlimb third trochanter landmark was palpated, and a 3 cm incision was made over the femur. The white band of fat and fascia over the femur was dissected to separate the vastus lateralis and biceps femoris muscles (Figure S7A, Supporting Information). Care was taken not to probe medially or caudally to avoid injury to the femoral artery and sciatic nerve, respectively. The femur was isolated using a micro spatula placed underneath to protect the soft tissues and to act as a skin retractor (Figure S7B,C, Supporting Information). A rotating circular saw blade (botiss biomaterials, Germany) was used to make a partial cut at the proximal and distal extents of the osteotomy. The proximal extent was half-way along the third trochanter, with attempt to preserve as much gluteal muscle attachment as possible. The distal cut was at the distal extent of the third trochanter, where a white triangular mark in the bone tapers off, visible during surgery, whereby removing a 2–3 mm piece of bone (Figure S7D, Supporting Information). Irrigation with sterile saline during bone cutting prevented thermal necrosis and aided removal of bone debris. Bleeding was minimal from the musculature and marrow cavity. A 25-gauge needle with the bevel removed with wire stripping pliers, bent at 4 mm length and autoclaved, was used to clear 4 mm depth within the marrow cavity of the proximal and distal femur prior to insertion of the polyimide pin (Figure S6, Supporting Information). The polyimide pin within the scaffold/collagen sponge, was inserted into the proximal and distal portion of the femur (Figure S7E,F, Supporting Information). The PCL-TMA900 scaffold or collagen sponge construct was assessed to be correctly positioned within the defect (Figures S7G and S8, Supporting Information). The muscle layer was closed with two simple interrupted sutures with 5/0 PDS (Ethicon, USA) (Figure S7H, Supporting Information). The skin was closed in a simple interrupted, horizontal mattress suture pattern using 5/0 PDS (Ethicon, USA), with the knots toward the tail to prevent interference by the mouse (Figure S7I, Supporting Information). Following µCT imaging, the mice were recovered in a warming cage (Thermacage, datesand, UK) postoperatively until alert and mobile and returned to their IVC cage. Food was offered from the cage floor to prevent the necessity of standing on the back legs to reach the food hopper, and behavior, mobility and nesting behavior were monitored. Buprenorphine (0.05 mg kg^{-1}) was administered by subcutaneous injection 6–8 h postoperatively and continued twice daily for 3 days. Of note, in the current study, the scaffold was firmly attached to the proximal femur with the pin held straight within the medullary canal and scaffold in this region, creating a pivot point for the plastic pin to bend and to be held there under the adductor muscle force, compared to the second pilot study where the plastic pin bent at the edge of the proximal femur and therefore remained straight within the scaffold and distal portion of the femur, thereby maintaining a relatively straight limb. Use of a barbed pin to grip the endosteum of the diaphysis could perhaps improve stability and placement of the IM pin.[40] There was a change in direction of the greater trochanter of the femur, from a lateral position to a cranial position, in all mice in all studies performed, due to the unavoidable disruption of the surrounding musculature at surgery, however, this did not appear to interfere with locomotion.

© 2024 The Author(s). Advanced Materials Interfaces published by Wiley-VCH GmbH

21967350, 2025, 1, Downloaded from https://onlinelibrary.wiley.com/doi/10.1002/admi.202400389 by Imperial College London, Wiley Online Library on [17/01/2025]. See the Terms and Conditions (https://onlinelibrary.wiley.com/terms-and-conditions) on Wiley Online Library for rules of use; OA articles are governed by the applicable Creative Commons License

μCT Procedure and Analysis: Micro-CT was performed using a MILabs OI-CTUHXR preclinical imaging scanner (Utrecht, The Netherlands). General anesthesia was induced in an induction chamber with 5% Isoflurane (VetTech) and 100% oxygen (0.8 L min^{-1} flow rate), followed by maintenance of general anesthesia at approximately 1.5–2% isoflurane throughout imaging, with the oxygen rate constant at ≈1.0 L min^{-1}. BioVet software connected to the Milabs scanner permitted monitoring of respiratory activity (minimum of 60 breaths per minute to judge anesthetic depth) and setting the temperature of the scanning bed to 34 °C. Lubrithal (Dechra, UK) was applied to both eyes to prevent corneal desiccation. Mice were imaged from the mid back to the hindlimb digits, typically 2 μCT bed positions were selected, with a total scan time of approximately 10 min per acquisition. The mice recovered on 100% oxygen, while being kept warm on the imaging bed. After signs of movement were observed, the mouse was transferred to a warming box (Thermacage, datesand, UK) prewarmed at 30 °C until normal mouse activity resumed (eating, walking, grooming) at which point the mouse was returned to IVC cage housing.

The mice underwent μCT scanning on the day of surgery and at 2, 4, 6, and 8 weeks postsurgery. Scanning at the 8-week time point was performed postmortem and included ex vivo hindlimbs (Table S2). μCT reconstructions were obtained using MILabs software (MILabs-Recon v. 11.00) at 40 × 10^{-6} and 20 × 10^{-6} m resolution for in vivo and ex vivo images, respectively. Formation of skeletal tissue was assessed using Imalytics Preclinical software v3.0 (Gremse-IT GmbH) and a gauss filter of 1.0 was applied in each method of analysis. A bone density phantom was scanned at each time point using identical parameters as a reference for bone density quantification to enable a minimum threshold to be set for bone volume analysis.

For analysis, segmentation of the region of interest was performed at all timepoints. Initially analysis of a segment of bone from proximal to distal femur was quantified for an overall view of bone formation in each group (Figure S9, Supporting Information). Further focused analysis was performed by selecting a 4 mm diameter 6 mm length cylindrical volume over the scaffold (scaffold size 3 mm diameter × 5 mm length), therefore including a 0.5 mm periphery around scaffold. The center of the scaffold was measured to be 2.5 mm from the femur ends and 1.5 mm from the perceived edge of the scaffold. This was most accurate in ex vivo images due to enhanced detail of the radiolucent scaffold against the surrounding soft tissues (Figure S10, Supporting Information). The cylindrical volume was applied to the scaffold (Figure S11A, Supporting Information). For collagen sponge, the 4 mm diameter × 6 mm length cylinder was used with 0.5 mm of both sides of the femur included in analysis as this was equivalent to the limbs with the scaffolds to avoid underestimation of bone volume. Nevertheless, the bone volume would be difficult to equivocate to the PCL-TMA900 scaffolds as the diameter of the collagen sponge swelled to greater than 4 mm, so the outer bone was disregarded from quantification (Figure S11B, Supporting Information).

To analyze the volume of bone formed on the scaffold a 3 mm diameter × 5 mm length cylinder was selected, and bone volume quantified in the ex vivo images at week 8, permitting enhanced visualization of the shape of bone formed within the scaffold (Figure S12A, Supporting Information). In the case of the collagen sponge, the 3 × 5 mm cylindrical volume was selected, and the femur ends removed from the bone quantification as the sponge were compressed to bring the femur ends within the 3 × 5 mm volume, which would lead to overestimation of bone volume. Again, the outer bone which formed wider than 3 mm diameter was disregarded from analysis (Figure S12B, Supporting Information).

The medial and lateral sides of the most efficacious scaffolds; ELP/PEA/FN/BMP-2, PEA/FN/BMP-2 and Laponite/BMP-2 coated scaffolds were quantified by creating a cylinder (1.5 × 5 mm) medial and lateral within the 3 × 5 mm scaffold cylinder volume (Figure S13A–F, Supporting Information). The cylinder was positioned over the medial and lateral scaffold respectively by lining up the image in all 2D planes. The medial and lateral volumes were segmented out and quantified individually (Figure S13G,H, Supporting Information).

Histological Processing, Embedding, and Sectioning of Mouse Limbs: The polyimide IM pin was not removed from each limb as the IM pin was amenable to processing, embedding, and sectioning (Figure S14, Supporting Information). Samples were fixed in 4% PFA for 3–4 days, rinsed in PBS and decalcified for 4 weeks with 5% ethylenediaminetetraacetic acid (EDTA) in 0.1 m Tris in dH_2O (pH 7.3 with NaOH) at 4 °C on the rotator. The decalcification solution was changed weekly, and μCT/X-ray confirmed complete decalcification prior to rinsing in PBS and dehydration. After dehydration through ethanol solutions (70%, 90%, 100% twice) and chloroform:100% ethanol mix in a 1:1 ratio, followed by 100% chloroform twice, for 1 h in each solution, the samples were processed in the Heraeus Vacutherm VT6025 Vacuum Oven in molten paraffin wax (Histowax, Leica) at 65 °C for 1 h. Fresh wax was added and a further 2 h in the vacuum oven commenced. The samples were embedded in fresh molten wax and cooled at 0–1 °C for 2 h before storage at 4 °C. The blocks were sectioned at 10 × 10^{-6} m on a Microm 330 microtome (Optec, UK). The sections were transferred via a water bath to pre-heated glass slides for 2 h until dry and placed in the slide oven at 37 °C for 4–6 h prior to storage at 4 °C.

Histological Staining of Tissues—Alcian Blue/Sirius Red: The method was extrapolated from Marshall et al.[9] The tissue sections on slides were rehydrated through Histoclear (2 × 7 min), ethanol solutions of 100% (twice) to 90% to 50% (2 min each), followed by immersion in water. Weigert's hematoxylin was applied for 10 min, removed by immersion three times in acid/alcohol (5% HCl/70% ethanol) followed by washing in the water bath for 5 min. Slides were immersed in 0.5% Alcian blue 8GX in 1% acetic acid for 10 min, 1% molybdophosphoric acid for 10 min, followed by rinsing with water prior to staining with 1% Picrosirius Red (Sirius Red) for 1 h. Excess stain was rinsed off in water and the slides were dehydrated in increasing concentrations of ethanol of 50%, 90%, 100% twice, and Histoclear twice for 30 s in each, prior to mounting with DPX and a glass coverslip and air-dried.

Histological Staining of Tissues—Goldner's Trichrome: The method was extrapolated from Marshall et al.[9] The method followed is identical to Alcian blue/Sirius Red staining to the stage of acid/alcohol immersion and washing in water for 5 min. Ponceau Acid Fuchsin/Azophloxin (Sigma) was applied for 5 min followed by a 15 s wash in 1% acetic acid. Phosphomolybdic acid/Orange G was applied for 20 min followed by another 15 s wash in 1% acetic acid. Light Green was applied for 5 min followed by the third 15 s wash in 1% acetic acid. The sections on the slides were dehydrated in ethanol 90% and 100% twice and Histoclear twice for 30 s each prior to mounting with DPX and a glass coverslip and air-dried.

Tartrate-Resistant Acid Phosphatase (TRAP) Staining: For the visualization of osteoclast activity, TRAP Basic Incubation Medium (9.2 g sodium acetate anhydrous, 11.4 g l-tartaric acid, 950 mL dH_2O, 2.8 mL glacial acetic acid, pH adjusted with 5 m sodium hydroxide to pH 4.7–5.0 and made up to 1 L with dH_2O and Naphthol AS-MX Phosphate substrate (2 mg Naphthol AS-MX Phosphate to 0.1 mL of ethylene glycol monoethyl ether) were prepared. The final staining solution was prepared from 20 mL of TRAP basic incubation medium, 0.1 mL of Naphthol AS-MX Phosphate substrate and 12 mg of Fast Red Violet LB Salt, prewarmed to 37 °C in a drying oven. The slides were dewaxed and rehydrated prior to staining with TRAP staining solution applied to each slide and incubated at 37 °C for 30 min, checking red positive stain development on positive control slides. The slides were rinsed in dH_2O and counterstained with 0.02% Fast Green stain for 30 s, rinsed in dH_2O, dehydrated through 50%, 90%, 100% (twice), and Histoclear (twice) for 30 s in each solution. Slides were mounted with DPX and a glass cover slip applied and allowed to dry.

Image Acquisition of Histology Slides: Histological wax samples were imaged using the Zeiss Axiovert 200 microscope using bright field microscopy and images captured with the Axiovision 4.2 imaging software (Zeiss).

Statistical Analysis: Data from replicates were analyzed using on GraphPad Prism 9, version 9.2.0. p values <0.05 were considered significant. Graphical representation of significance as follows: $^{*}p < 0.05$, $^{**}p < 0.01$, $^{***}p < 0.001$, $^{****}p < 0.0001$. All data presented as mean and standard deviation (S.D.).

© 2024 The Author(s). Advanced Materials Interfaces published by Wiley-VCH GmbH

21967350, 2025, 1, Downloaded from https://onlinelibrary.wiley.com/doi/10.1002/admi.202400389 by Imperial College London, Wiley Online Library on [17/01/2025]. See the Terms and Conditions (https://onlinelibrary.wiley.com/terms-and-conditions) on Wiley Online Library for rules of use; OA articles are governed by the applicable Creative Commons License

Supporting Information

Supporting Information is available from the Wiley Online Library or from the author.

Received: May 5, 2024
Revised: October 25, 2024
Published online: November 21, 2024

Acknowledgements

Research support for this study from the Biotechnology and Biological Sciences Research Council (BBSRC BB/P017711/1), the UK Regenerative Medicine Platform Acellular / Smart Materials – 3D Architecture (MR/R015651/1), ERC Proof-of-concept grant MINGRAFT, and University of Southampton is gratefully acknowledged as well as many useful discussions with current members of the Bone and Joint Research Group in Southampton, UK. The authors thank Professor Nicholas Evans and Dr. Yanghee Kim University of Southampton, for helpful discussions on the program of work. Dr. Katie Dexter, University of Southampton Biomedical Imaging Unit, is acknowledged for advice in μCT scanning of mice and thanks to Professor Nicholas Evans, Dr. Roxanna Ramnarine Sanchez and Mr. Andrew Rawlings, at the University of Southampton, for their assistance during the final in vivo study. S.J.P.C. acknowledges funding through a Rubicon fellowship from the Dutch Research Council (File No. 019.211EN.025) and through a UKRI Postdoctoral Fellowship (EP/X027163/1). M.M.S. acknowledges support from the NIHR (NIHR133314). Dr. Akemi Nogiwa Valdez is acknowledged for proof reading of the manuscript. For the purpose of open access, the author has applied a "Creative Commons Attribution"(CC BY) license to any Author Accepted Manuscript version arising.

Conflict of Interest

R.O.C.O. and J.I.D. are co-founders and shareholders in a University spin out company with a license to IP indirectly related to the current manuscript. M.M.S. reports financial support was provided by UK Regenerative Medicine Platform, and she invested in, consults for (or is on scientific advisory boards or boards of directors) and conducts sponsored research funded by companies related to the biomaterials field. All other authors declare that they have no known competing financial interests or personal relationships that could have appeared to influence the work reported in this paper.

Author Contributions

S.J.P.C. designed and modeled the scaffolds. C.E. and J.P.W. produced the PCL-TMA900 resin. J.P.W. and T.Y. prepared and printed the PCL-TMA900 scaffolds. V.J. extrusion printed the PCL scaffolds for the first pilot study, performed PEA coating of scaffolds and organized the EO sterilization of materials. A.H. ELP coated the scaffolds. J.I.D. supplied the Laponite and edited the paper. K.M.M. was responsible for conceptualization of the study methods and conducted the in vivo experiments, data collection and analysis, histology, and wrote the paper. J.M.K, A.M., M.S.-S., M.M.S., and R.O.C.O. were responsible for conceptualization, funding acquisition, study supervision, and editing of the manuscript.

Data Availability Statement

The data that support the findings of this study are available from the corresponding author upon reasonable request.

Keywords

bioactive, biomaterial, bone tissue engineering, femur defect model, Laponite

[1] G. Fernandez de Grado, L. Keller, Y. Idoux-Gillet, Q. Wagner, A. M. Musset, N. Benkirane-Jessel, F. Bornert, D. Offner, *J. Tissue Eng.* **2018**, *9*, 2041731418776819.
[2] J. F. Keating, A. H. R. W. Simpson, C. M. Robinson, *J. Bone Jt. Surg.* **2005**, *87*, 142.
[3] H. Shegarfi, O. Reikeras, *OSJ* **2009**, *17*, 206.
[4] H. J. Haugen, S. P. Lyngstadaas, F. Rossi, G. Perale, *J. Clin. Periodontol.* **2019**, *46*, 92.
[5] A. R. Amini, C. T. Laurencin, S. P. Nukavarapu, *Crit. Rev. Biomed. Eng.* **2012**, *40*, 363.
[6] C. S. Bahney, D. P. Hu, T. Miclau, R. S. Marcucio, *Front. Endocrinol.* **2015**, *6*, 4.
[7] S. Basyuni, A. Ferro, V. Santhanam, M. Birch, A. McCaskie, *Br. J. Oral Maxillofac. Surg.* **2020**, *58*, 632.
[8] K. M. Marshall, J. P. Wojciechowski, C. Echalier, S. J. P. Callens, T. Yang, Ø. Øvrebø, K. Zhou, V. Jayawarna, J. M. Kanczler, M. M. Stevens, J. I. Dawson, R. O. C. Oreffo, *Adv. Mater. Interfaces* **2024**, *11*, 2400332.
[9] K. M. Marshall, J. P. Wojciechowski, V. Jayawarna, A. Hasan, C. Echalier, Ø. Øvrebø, T. Yang, K. Zhou, J. M. Kanczler, A. Mata, M. Salmeron-Sanchez, M. M. Stevens, R. O. C. Oreffo, *Sci Rep* **2024**, *14*, 25832.
[10] B. Gaihre, M. D. A. Potes, X. Liu, M. Tilton, E. Camilleri, A. Rezaei, V. Serdiuk, S. Park, F. Lucien, A. Terzic, L. Lu, *J. Biomed. Mater. Res., Part A* **2023**, *112*, 672.
[11] A. Girotti, A. Fernandez-Colino, I. M. Lopez, J. C. Rodriguez-Cabello, F. J. Arias, *Biotechnol. J.* **2011**, *6*, 1174.
[12] S. Elsharkawy, M. Al-Jawad, M. F. Pantano, E. Tejeda-Montes, K. Mehta, H. Jamal, S. Agarwal, K. Shuturminska, A. Rice, N. V. Tarakina, R. M. Wilson, A. J. Bushby, M. Alonso, J. C. Rodriguez-Cabello, E. Barbieri, A. Del Rio Hernandez, M. M. Stevens, N. M. Pugno, P. Anderson, A. Mata, *Nat. Commun.* **2018**, *9*, 2145.
[13] A. Hasan, R. Bagnol, R. Owen, A. Latif, H. M. Rostam, S. Elsharkawy, F. Rose, J. C. Rodriguez-Cabello, A. M. Ghaemmaghami, D. Eglin, A. Mata, *Front. Bioeng. Biotechnol.* **2022**, *10*, 836386.
[14] X. Wei, J. Chen, H. Y. Shen, K. Jiang, H. Ren, Y. Liu, E. Luo, J. Zhang, J. Z. Xu, Z. M. Li, *Adv. Healthcare Mater.* **2024**, *13*, 2304178.
[15] H. Y. Shen, F. Xing, S. Y. Shang, K. Jiang, M. Kuzmanovic, F. W. Huang, Y. Liu, E. Luo, M. Edeleva, L. Cardon, S. Huang, Z. Xiang, J. Z. Xu, Z. M. Li, *ACS Appl. Mater. Interfaces* **2024**, *16*, 18658.
[16] Z. A. Cheng, A. Alba-Perez, C. Gonzalez-Garcia, H. Donnelly, V. Llopis-Hernandez, V. Jayawarna, P. Childs, D. W. Shields, M. Cantini, L. Ruiz-Cantu, A. Reid, J. F. C. Windmill, E. S. Addison, S. Corr, W. G. Marshall, M. J. Dalby, M. Salmeron-Sanchez, *Adv. Sci.* **2019**, *6*, 1800361.
[17] D. J. Page, C. E. Clarkin, R. Mani, N. A. Khan, J. I. Dawson, N. D. Evans, *Acta Biomater.* **2019**, *100*, 378.
[18] J. I. Dawson, J. M. Kanczler, X. B. Yang, G. S. Attard, R. O. Oreffo, *Adv. Mater.* **2011**, *23*, 3304.
[19] D. M. Gibbs, C. R. Black, G. Hulsart-Billstrom, P. Shi, E. Scarpa, R. O. Oreffo, J. I. Dawson, *Biomaterials* **2016**, *99*, 16.
[20] R. S. Ramnarine-Sanchez, J. M. Kanczler, N. D. Evans, R. O. C. Oreffo, J. I. Dawson, *Adv. Mater.* **2023**, *35*, 2304461.
[21] Y. Hou, W. Wang, P. Bartolo, *Mater. Today Bio* **2024**, *24*, 100886.
[22] R. Xue, X. Deng, X. Xu, Y. Tian, A. Hasan, A. Mata, L. Zhang, L. Liu, *Biomater. Adv.* **2023**, *151*, 213471.
[23] Z. J. Gunderson, Z. R. Campbell, M.cK. TO, R. M. Natoli, M. A. Kacena, *Injury* **2020**, *51*, 1439.

© 2024 The Author(s). Advanced Materials Interfaces published by Wiley-VCH GmbH

21967350, 2025, 1, Downloaded from https://onlinelibrary.wiley.com/doi/10.1002/admi.202400389 by Imperial College London, Wiley Online Library on [17/01/2025]. See the Terms and Conditions (https://onlinelibrary.wiley.com/terms-and-conditions) on Wiley Online Library for rules of use; OA articles are governed by the applicable Creative Commons License

[24] T. Rocha, A. S. Cavalcanti, A. C. Leal, R. B. Dias, R. S. da Costa, G. O. Ribeiro, J. A. M. Guimaraes, M. E. L. Duarte, *Injury* **2021**, *52*, S3.
[25] L. Findeisen, J. Bolte, C. Vater, C. Petzold, M. Quade, L. Muller, S. B. Goodman, S. Zwingenberger, *BMC Musculoskeletal Disord.* **2021**, *22*, 401.
[26] M. Manassero, V. Viateau, R. Matthys, M. Deschepper, R. Vallefuoco, M. Bensidhoum, H. Petite, *Tissue Eng., Part C* **2013**, *19*, 271.
[27] K. Liu, D. Li, X. Huang, K. Lv, D. Ongodia, L. Zhu, L. Zhou, Z. Li, *J. Surg. Res.* **2013**, *183*, 493.
[28] P. Tiyapatanaputi, P. T. Rubery, J. Carmouche, E. M. Schwarz, R. J. O'Keefe, X. Zhang, *J. Orthop. Res.* **2004**, *22*, 1254.
[29] A. Lang, A. Schulz, A. Ellinghaus, K. Schmidt-Bleek, *Lab. Anim.* **2016**, *50*, 433.
[30] S. Zwingenberger, E. Niederlohmann, C. Vater, S. Rammelt, R. Matthys, R. Bernhardt, R. D. Valladares, S. B. Goodman, M. Stiehler, *J. Surg. Res.* **2013**, *181*, e7.
[31] H. Uusitalo, J. Rantakokko, M. Ahonen, T. Jamsa, J. Tuukkanen, V.-M. Kahari, E. Vuorio, H. T. Aro, *Bone* **2001**, *28*, 423.
[32] J. M. Kanczler, P. J. Ginty, L. White, N. M. Clarke, S. M. Howdle, K. M. Shakesheff, R. O. Oreffo, *Biomaterials* **2010**, *31*, 1242.
[33] M. Zarek, N. Mansour, S. Shapira, D. Cohn, *Macromol. Rapid Commun.* **2017**, *38*, 1600628.
[34] B. J. Green, K. S. Worthington, J. R. Thompson, S. J. Bunn, M. Rethwisch, E. E. Kaalberg, C. Jiao, L. A. Wiley, R. F. Mullins, E. M. Stone, E. H. Sohn, B. A. Tucker, C. A. Guymon, *Biomacromolecules* **2018**, *19*, 3682.
[35] I. Chung, D. Xie, A. D. Puckett, J. W. Mays, *Eur. Polym. J.* **2003**, *39*, 1817.
[36] K. D. G. Samson, V. Hidalgo-Alvarez, T. R. Dargaville, M. F. P. W. Tough, *Adv. Funct. Mater.* **2023**, *33*, 2213797.
[37] J. Field, J. W. Haycock, F. M. Boissonade, C. F. A. Tuneable, *Photocurable Mol.* **2021**, *26*, 1199.
[38] F. S. L. Bobbert, K. Lietaert, A. A. Eftekhari, B. Pouran, S. M. Ahmadi, H. Weinans, A. A. Zadpoor, *Acta Biomater.* **2017**, *53*, 572.
[39] A. Alba-Perez, V. Jayawarna, P. G. Childs, M. J. Dalby, M. Salmeron-Sanchez, *Mater. Sci. Eng., C* **2020**, *113*, 110966.
[40] B. H. Clough, M. R. McCarley, C. A. Gregory, *J. Visualized Exp.* **2015**, e52368.
[41] W. G. Marshall, C. Gonzalez-Garcia, S. Trujillo, A. Alba-Perez, P. Childs, D. W. Shields, A. Tomlinson, R. Pettitt, B. Filliquist, P.-Y. Chou, M. J. Dalby, S. A. Corr, M. Salmeron-Sanchez, *VCOT Open* **2023**, *06*, e41.
[42] C. Xu, T. Lin, X. Zhao, Y. Gan, J. Huang, J. Zhang, H. Zheng, C. Pu, R. Lin, B. Yan, G. Hu, Q. Liu, B. Yu, S. Li, H. Hou, *Composites, Part B* **2023**, *259*, 110726.
[43] S. Huo, Z. Lyu, X. Su, F. Wang, J. Liu, S. Liu, X. Liu, X. Bao, J. Zhang, K. Zheng, G. Xu, *Composites, Part B* **2023**, *253*, 110521.
[44] Y. Y. Yu, S. Lieu, C. Lu, C. Colnot, *Bone* **2010**, *47*, 65.
[45] J. M. Kanczler, S. H. Mirmalek-Sani, N. A. Hanley, A. L. Ivanov, J. J. Barry, C. Upton, K. M. Shakesheff, S. M. Howdle, E. N. Antonov, V. N. Bagratashvili, V. K. Popov, R. O. Oreffo, *Acta Biomater.* **2009**, *5*, 2063.
[46] J. M. Kanczler, P. J. Ginty, J. J. Barry, N. M. Clarke, S. M. Howdle, K. M. Shakesheff, R. O. Oreffo, *Biomaterials* **2008**, *29*, 1892.
[47] E. Wehrle, D. C. Tourolle Ne Betts, G. A. Kuhn, A. C. Scheuren, S. Hofmann, R. Muller, *Sci. Rep.* **2019**, *9*, 17445.
[48] A. Kaur, S. Mohan, C. H. Rundle, *Anim. Models Exp. Med.* **2020**, *3*, 130.
[49] X. Chen, J. Guo, Y. Yuan, Z. Sun, B. Chen, X. Tong, L. Zhang, C. Shen, J. Zou, *Mol. Med. Rep.* **2017**, *15*, 2890.
[50] P. Augat, M. Hollensteiner, C. von Ruden, *Injury* **2021**, *52*, S78.
[51] R. W. Hente, S. M. Perren, *J. Biomech.* **2021**, *125*, 110576.
[52] M. Windolf, M. Ernst, R. Schwyn, D. Arens, S. Zeiter, *Injury* **2021**, *52*, 71.
[53] S. Schreivogel, V. Kuchibhotla, P. Knaus, G. N. Duda, A. Petersen, *J. Tissue Eng. Regener. Med.* **2019**, *13*, 1992.
[54] L. Claes, *J. Biomech.* **2021**, *115*, 110148.
[55] M. He, L. Li, Y. Liu, Z. Wu, Y. Xu, L. Xiao, K. Luo, X. Xu, *Int. J. Biol. Macromol.* **2024**, *276*, 133775.
[56] K. M. Marshall, J. S. McLaren, J. P. Wojciechowski, S. J. P. Callens, C. Echalier, J. M. Kanczler, F. Rose, M. M. Stevens, J. I. Dawson, R. O. C. Oreffo, *Biomater. Adv.* **2024**, *164*, 213959.

© 2024 The Author(s). Advanced Materials Interfaces published by Wiley-VCH GmbH

21967350, 2025, 1, Downloaded from https://onlinelibrary.wiley.com/doi/10.1002/admi.202400389 by Imperial College London, Wiley Online Library on [17/01/2025]. See the Terms and Conditions (https://onlinelibrary.wiley.com/terms-and-conditions) on Wiley Online Library for rules of use; OA articles are governed by the applicable Creative Commons License